5-2019

Structural Control of Thermal Fluid Circulation and Geochemistry in a Flat-Slab Subduction Zone, Peru

Brandt E. Scott
Utah State University

STRUCTURAL CONTROL OF THERMAL FLUID CIRCULATION AND GEOCHEMISTRY IN A FLAT-SLAB SUBDUCTION ZONE, PERU

by

Brandt E. Scott

A thesis submitted in partial fulfillment
of the requirements for the

of

MASTER OF SCIENCE

in

Geology

Approved:

Dennis Newell, Ph.D. Major Professor	Alexis Ault, Ph.D. Committee Member
Anthony Lowry, Ph.D. Committee Member	Richard S. Inouye, Ph.D. Vice Provost for Graduate Studies

UTAH STATE UNIVERSITY
Logan, Utah

2019

ABSTRACT

Structural Control of Thermal Fluid

Circulation and Geochemistry in a

Flat-Slab Subduction Zone, Peru

by

Brandt Scott, Master of Science

Utah State University, 2019

Major Professor: Dr. Dennis L. Newell
Department: Geology

Thermal spring geochemistry from the Cordillera Blanca and Huayhuash ranges in Peru reveal the influence of lithospheric-scale structures on hydrothermal fluid circulation. To test the influence of a major structure, such as the Cordillera Blanca detachment fault, thermal springs were targeted along the trace of the detachment fault (Group 1), within the hanging-wall of the fault (Group 2; western edge of Cordillera Blanca), on the east side of the Cordillera Blanca mountain range (Group 3), and in the Cordillera Huayhuash range (Group 4). Water and dissolved gas samples were acquired from all springs and analyzed for a suite of natural chemical and isotopic tracers. Group 1 and 2 springs yield dominantly brackish–saline, alkaline-chloride waters, with $\delta^{18}O_{SMOW}$ (−14.7 to −4.9 ‰) and δD_{SMOW} (−113 to −74 ‰) values that suggest mixing with an isotopically distinct brine at depth. Cl/Br ratios in Group 1 and 2 springs are generally greater than seawater (> 647) and also

support mixing with deep Cl-rich brine. In contrast, springs from Groups 3 and 4 exhibit a wide range of water types and plot along the global meteoric water line, suggesting a greater influence from shallow groundwater. Cl/Br ratios from Group 3 and 4 springs are typically lower than seawater (< 647) and are consistent with a dominant meteoric influence. A relatively narrow range of $\delta^{13}C_{PDB}$ values (-10.8 to -6.3 ‰) for dissolved inorganic carbon in Group 1 and 2 springs suggest mixing between organic and mantle/crustal carbon, compared to the wider range (-12.6 to -1.8 ‰) in Group 3 and 4 springs that indicate the influence of marine carbonate-derived carbon. Calculated geothermometry temperatures of 91 to 226° C indicate deep flow-paths (up to 10 km) associated with Groups 1 and 2. Alternatively, Groups 3 and 4 yield geothermometry temperatures (40 – 98° C) that correspond to much shallower circulation (< 4 km), likely explaining the geochemical differences between Groups 3 and 4 versus Groups 1 and 2. Collectively, these datasets suggest that a network of permeability pathways between springs along the detachment (Group 1) and in its hanging-wall (Group 2) act as a structural control on hydrothermal fluids and accommodates deep fluid circulation.

(72 pages)

PUBLIC ABSTRACT

Structural Control of Thermal Fluid
Circulation and Geochemistry in a
Flat-Slab Subduction Zone, Peru

Brandt Scott

Hot spring geochemistry from the Peruvian Andes provide insight on how faults, or fractures in the Earth's crust, are capable of influencing fluid circulation. Faults can either promote or inhibit fluid flow and the goal of this study is test the role of a major fault, such as the Cordillera Blanca detachment, as a channel for transporting deep fluids to the surface. Hot springs are abundant in the Cordillera Blanca and Huayhuash ranges in Peru, and several springs issue along the Cordillera Blanca detachment, making this region an ideal setting for our study. To test the role of the Cordillera Blanca detachment, hot springs were sampled along the trace of the fault (Group 1), the western edge of the Cordillera Blanca (Group 2), the eastern side of the Cordillera Blanca (Group 3), and in the Cordillera Huayhuash (Group 4). Water and dissolved gas samples were collected from a total of 25 springs and then analyzed for an array of geochemical parameters. Distinct fluid chemistries from Groups 1 and 2 suggest that the Cordillera Blanca detachment and adjacent minor faults to the west intersect at depth and provide a preferential flow path for deep fluid circulation. Understanding the influence of faults on fluid flow is essential for

many disciplines (e.g. oil exploration, hydrology), and this work demonstrates that fluid geochemistry is an excellent tool for assessing the role of faults on fluid distribution.

ACKNOWLEDGMENTS

First and foremost, I would like to acknowledge all the faculty of the Utah State Geology Department. Our personable and thought-provoking professors always know how to stimulate discussion and motivate students to their greatest potential. Having access to such a close-knit community that I could depend on or reach out to truly allowed me to succeed at Utah State.

Next, I would like to acknowledge all the individuals that helped make this study possible. The members of our 2017 field campaign: Micah Jessup and Tyler Grambling from the University of Tennessee, Knoxville. Thank you for traversing the Peruvian Andes with me in search of hot springs with ambiguous localities. To our Peruvian geography guide, Alberto Cafaratta (Pony's Expeditions), we owe a big part of our success in the field to your extensive knowledge of Peru. Thank you to the individuals that assisted with geochemical analyses: Andrew Lonero, Jaime D. Barnes, and Tobias Fischer. Thank you to the members of my committee, Alexis Ault and Tony Lowry, for reviewing and providing constructive feedback on this thesis. And to my girlfriend, Meredith Westover, thank you for supporting me every step of my graduate school career.

Last, but certainly not least, I would like to thank Dennis Newell for going above and beyond as an academic advisor. I have learned an incredible amount working with you these past few years and I aspire to attain that perfect balance of mentor and friend that you exude so easily. Thank you for taking me on as a student and entrusting me with the continuation of your work. I hope our geologic career paths cross again in the future.

CONTENTS

Page

LIST OF TABLES

Table Page

LIST OF FIGURES

Figure Page

1. Introduction

1.1 Overview

Thermal springs emanating along faults provide a geochemical window into fluid provenance, circulation pathways, and the influence of faults on fluid migration. Faults can act as conduits or barriers to fluid flow, thereby affecting the distribution, circulation depth, and overall geochemistry of aqueous fluids in the continental lithosphere (Hooper, 1991; Caine et al., 1996; Bense and Person, 2006). For example, fracture systems can provide effective pathways for the deep circulation of meteoric water, and its return to the surface in a hot spring (Nelson et al., 2009). Chemical and isotopic tracers from hot springs reflect processes occurring along the flow-path and can constrain the influence of faults on fluid flow. Geochemical studies of hot springs along strike-slip fault systems (California, Kennedy et al., 1997; Anatolia, Turkey; Mutlu et al., 2008; Himalayas, Klemperer et al., 2013) demonstrate these faults can act as deep conduits, transferring mantle-derived fluids (mantle-He) to the surface, in the absence of active volcanism. In the case of an active extensional setting, $^{3}He/^{4}He$ ratios measured in hot springs from the Basin and Range of the western U.S. show the presence of mantle volatiles increasing with increasing strain rate and are attributed to transit along deeply-penetrating normal faults (Kennedy and van Soest, 2007).

A recent study measured up to 25% mantle-He from hot springs along the Cordillera Blanca detachment (CBD) fault in a modern day flat-slab subduction zone in Peru (Newell et al., 2015) (Figs. 1, 2). Unlike typical “steep” subduction, which generates melt in the mantle via slab dehydration, flat-slab subduction eliminates the mantle wedge

and suppresses arc volcanism (Barazangi and Isacks, 1976; Pilger, 1981; Gutscher et al., 2000; Ramos and Folguera, 2009). This amount of mantle-He is therefore unexpected for a flat-slab region devoid of magmatism over the last ~5 Ma (Giovanni et al., 2010; Newell et al., 2015; Margirier et al., 2016). Geophysical imaging from the Peruvian flat slab suggests tearing along part of the slab just north of the Nazca ridge, and the likely presence of upwelling asthenosphere into the tear region (Antonijevic et al., 2015). Mantle-He in the Cordillera Blanca is hypothesized to originate from either a tear-induced contact with the asthenosphere, or from slab-derived lithospheric mantle volatiles mobilized by metasomatic fluids (Newell et al., 2015). The mechanism and/or process responsible for transferring these deep-seated mantle volatiles to the surface is still largely unknown.

The CBD is a major structural control in the Cordillera Blanca, capable of either inhibiting or promoting the migration of deep-seated fluids. The goal of this study is to test the role of the CBD as a channel for fluid migration, transferring deeply sourced fluids (including mantle volatiles) to the surface. The penetration depth of the CBD is poorly constrained, with an interpreted depth of at least ~10 km based on microseismicity (Deverchere et al., 1989). However, the structure has exhumed mylonites with deformation temperatures and pressures suggesting penetration deeper than the brittle-ductile transition (>15 km) (Hughes et al., in review). To complement the limited geophysical data, we investigate aqueous and stable isotope geochemistry of thermal springs located along the trace of the CBD, the hanging-wall of the CBD, east of the Cordillera Blanca mountain range, and in the Cordillera Huayhuash. Springs along the fault trace and in the hanging-

wall of the CBD are hypothesized to connect to hydrothermal fluids in the fault zone via fault-controlled high permeability flow (Newell et al., 2015). In this contribution, we build on prior work along the CBD (Newell et al., 2015), with new aqueous, gas, and stable isotope geochemistry data from hot springs throughout the region. We frame the data as a function of geographic location, highlight notable differences and similarities between hot springs, and explore the potential influence of lithospheric-scale structures on deeply circulating fluids in the Peruvian Andes.

2. Geologic Setting

2.1 Cordillera Blanca and Cordillera Huayhuash

The Cordillera Blanca (CB) is a northwest trending massif that primarily comprises a Neogene granodiorite with lesser ignimbrites representing the last magmatic event to occur in this part of Peru (~5 Ma; Giovanni et al., 2010) (Fig. 2). Jurassic shales and phyllites, in addition to Cretaceous carbonates and quartzites, are primarily exposed on the eastern and southern margins of the CB (Fig. 2). There are also exposures of Jurassic and Cretaceous units capping the CB batholith (Giovanni et al., 2010). At the time of emplacement (~14 - 5 Ma; Margirier et al., 2016), the CB batholith intruded Jurassic and Cretaceous sedimentary rock, of the Eocene Marañon Fold and Thrust Belt (Megard, 1984; Petford and Atherton, 1996). Later compressional events (Quechua events) occurred at ~20 Ma, ~9 Ma, and ~6-3 Ma, interspersed with periods of tectonic quiescence and extension

(Megard, 1984). The west side of the CB is cut by the Cordillera Blanca detachment fault (CBD), which strikes roughly parallel to the batholith exposure.

The Cordillera Huayhuash (CH), ~60 km southeast and along strike of the CB, is an analogous massif exhibiting similar rock types, elevation, and tectonic history as the CB (Garver et al., 2005) (Fig. 2). Notably, the CB and CH contain the highest (Huascaran, 6,655 m) and second highest peaks (Nevado Yerupaja, 6,634 m) along the Peruvian Andes, respectively. The CH predominantly comprises Cretaceous carbonates with smaller amounts of Early-Mid Tertiary volcanic rocks, all intruded by Miocene granitic plutons (Coney, 1971; Garver et al., 2005). A chain of Miocene plutons can be traced from the CH, north into the CB, suggesting related intrusive events. Additionally, silicic volcanism at ~6 Ma, denoted the Puscanturpa volcanics, are exposed and correlated to Late Miocene Yungay volcanics in the CB (Garver et al., 2005). Similar geology and topography suggest that the CH is a southern extension of the CB, yet the CH apparently lacks extensive normal faulting analogous to the CBD (Fig. 2). This distinction and presence of thermal springs in the CH provide an excellent test for structural control on fluid circulation in active orogens.

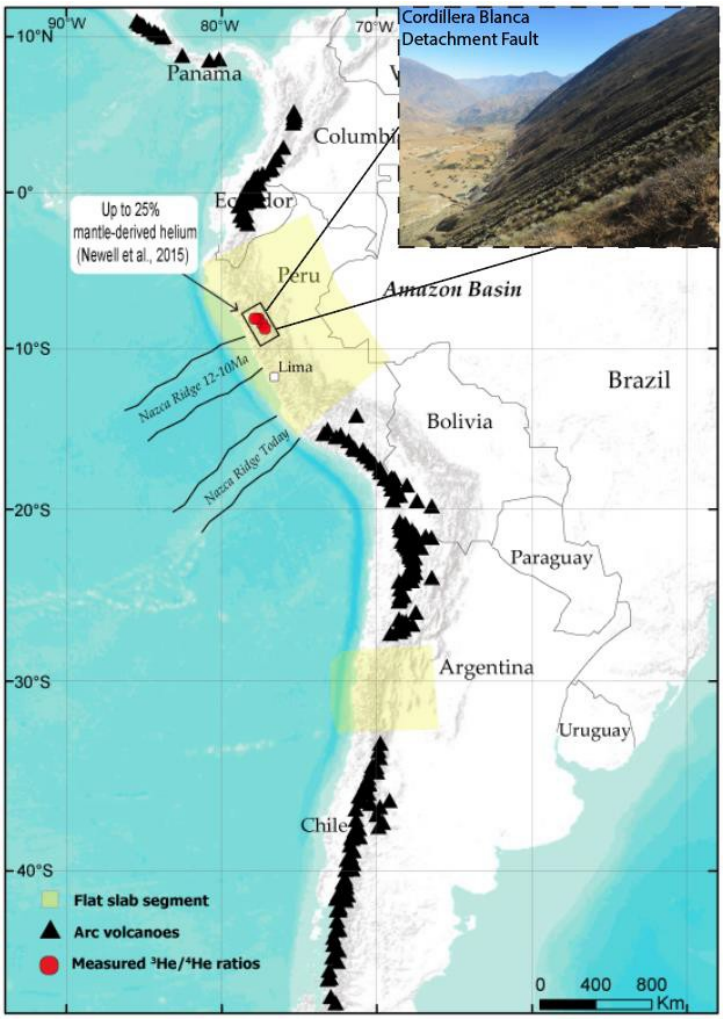

Figure 1. Variable subduction styles along the Andean arc, highlighted by arc volcanoes, interspersed with flat-slab segments. Black rectangle denotes study area where elevated $^{3}He/^{4}He$ ratios were measured from hot springs along the CBD (Newell et al., 2015). Inset displays extensive relief exhibited by the CBD (Photo: Dennis Newell).

2.2 Extension in the Cordillera Blanca

The NNW trending CBD extends ~200 km in length and dips WSW, ranging from 19° in the south to 36° in the north (Giovanni et al., 2010) (Fig. 2). Exposures of the detachment, north of Huaraz, exhibit mylonite zones and vertical relief up to 2.5 km

(Giovanni et al., 2010) (Figs. 1, 2). The fault breaks into smaller segments, terminating ~80 km to the SSE of Huaraz (Fig. 2). $^{40}Ar/^{39}Ar$ biotite dates from the hanging-wall indicate the onset of extension and faulting at ~5.4 Ma (Giovanni et al., 2010), followed by rapid batholith exhumation from ~5 to 2 Ma (Margirier et al., 2016).

Some research groups interpret CBD development as the result of gravitational collapse of a thickened crust (Deverchère et al., 1989; Petford and Atherton, 1992). This hypothesis however does not explain the lack of faulting in the CH, which is located southeast of the CB (~60 km) and exhibits a similar crustal thickness. Alternatively, extension and faulting along the CB may be linked to coupling of the overlying plate with the under-riding Nazca ridge at ~5 Ma (McNulty and Farber, 2002) (Fig. 1). This hypothesis proposes that buoyancy forces associated with the subducted Nazca ridge are sufficient to cause regional surface uplift and induce faulting. However, if the Nazca ridge subducted under the CB at ~15 Ma, then this challenges the veracity of the previous model (Rosenbaum et al., 2005; Margirier et al., 2015). Thermokinematic modeling of the final stages of batholith exhumation link intrusive-related strain in the western flanks of the CB with the initiation of the CBD at ~5.4 Ma (Margirier et al., 2016). Causes of extension in this subduction setting remain largely speculative and the initiation of the CBD is likely due to a combination of these factors. Regardless, the CBD is a significant structure in our study area and likely plays a major role in controlling the distribution of hydrothermal fluids.

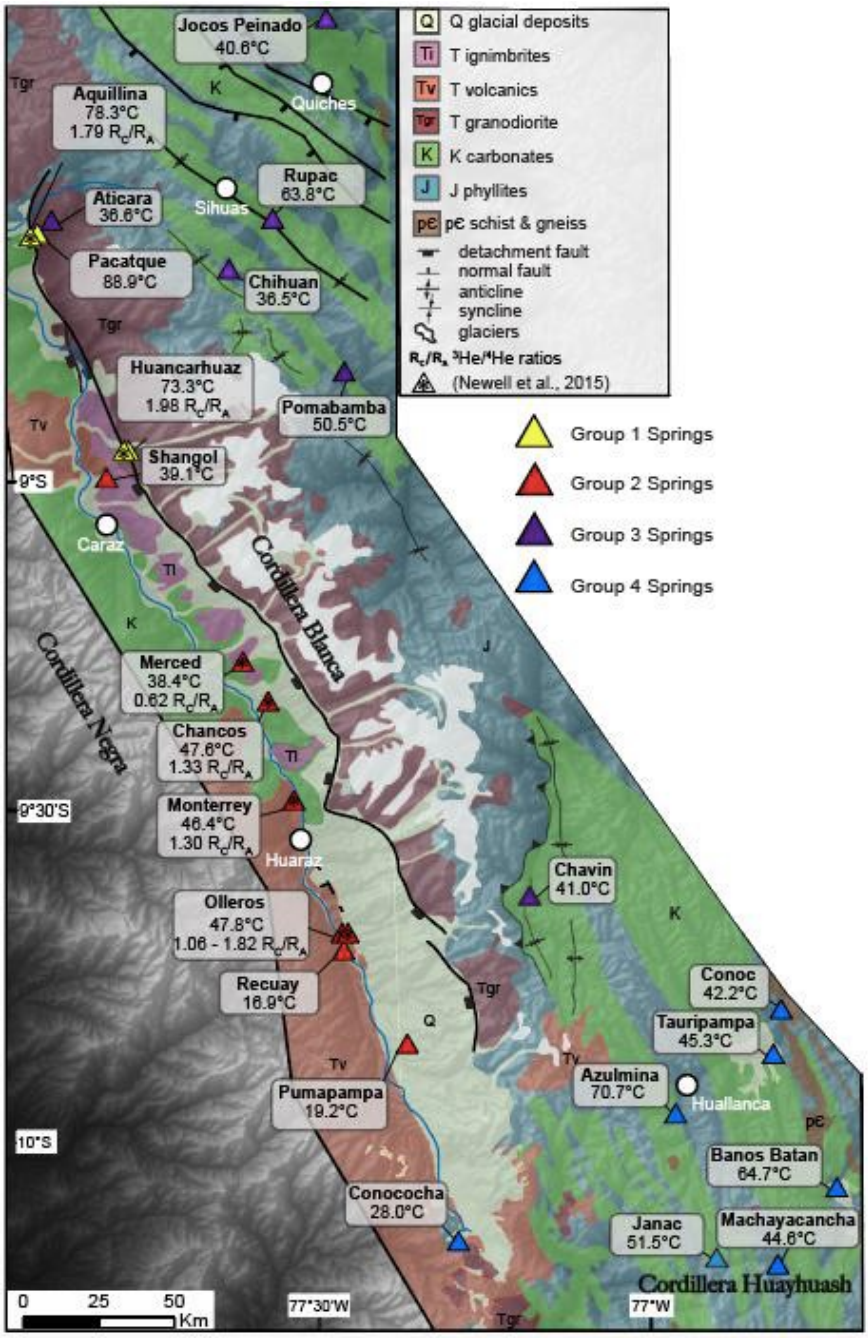

Figure 2. Thermal springs investigated along the Cordillera Blanca detachment (yellow triangles; Group 1), the hanging-wall (red triangles; Group 2), the footwall of the Cordillera Blanca (purple triangles; Group 3), and the Cordillera Huayhuash region (blue triangles; Group 4). These data are combined with previously published geochemistry data from the Cordillera Blanca (*) (Newell et al., 2015). Temperature, Cl isotope ratios, and $^{3}He/^{4}He$ (R_C/R_A) values are shown (this study; Newell et al., 2015). Surface geology modified from CB: Giovanni et al. (2010), CH: Cobbing et al. (1997).

3. Methods

3.1 Thermal spring sample targets and processes

New aqueous and stable isotope geochemistry data were acquired from 18 thermal springs located along the hanging-wall of the CBD, the footwall of the CBD, and the CH range (Fig. 2). These data are combined with previously published data from seven thermal springs along the trace and hanging-wall of the CBD (Newell et al., 2015). Here we report new geochemical data from 25 thermal springs in total, including duplicate samples from Baños Olleros and Baños Huancarhuaz (Table 1). To simplify the discussion of the results, we subdivide the springs into four groups based on geographic location. Group 1 (n = 4) are springs emanating along the trace of the CBD and Group 2 (n = 8) are springs located in the hanging-wall of the CBD (Fig. 2). Group 3 (n = 6) comprises springs to the east of the CB massif and Group 4 (n = 7) are springs located southward into the CH (Fig. 2). This subdivision allows us to objectively evaluate the role of lithospheric scale structures, like the CBD, on fluid pathways.

All springs were sampled as close to the source as possible to reduce the effect of cooling, degassing, atmospheric exchange, and evaporation at the surface. In several locations, we observed discharge as a group of spring emanations that may be controlled by a combination of localized structures and/or permeability variations. In these cases, field parameters (T, pH, conductivity) were used to screen sample locations, and generally the location with the highest temperature and/or conductivity was chosen for sampling (Table

1). Additional water samples were acquired at Baños (Huancarhuaz, Aquilina, Olleros, Pomabamba and Rupac) for oxygen and hydrogen stable isotope analysis (Table A4).

Techniques derived from methods used at volcanic arc settings and continental hydrothermal systems were used to sample thermal springs (e.g., Hilton et al., 2002). Temperature, pH, and conductivity of spring waters were measured in the field using an Oakton pH/cond/T portable meter (Fig. 3). Samples for water major and trace element chemistry, stable isotope ratios of oxygen, hydrogen, and chlorine were collected in 60 and 125-ml high-density polyethylene bottles (cation samples filtered with 0.45 μm disposable filters; anions and alkalinity collected unfiltered with no headspace). Cation samples were acidified with trace-metal grade HNO_3 in the lab immediately following fieldwork. Carbon stable isotope samples were collected in 30 ml amber glass vials with no headspace, and cold meteoric water was collected in 12 ml glass septa vials with no headspace. Water samples for helium isotope analyses and gas compositions were collected in ~12 X 3/8 in. O.D. annealed Cu tubing, cold-sealed with refrigeration clamps (Hilton et al., 2002) (Fig. 4).

Figure 3. Field measurement of temperature, pH, and conductivity using an Oakton portable meter at Baños Conococha.

Figure 4. Collection of water sample using Cu tubing equipped with refrigeration clamps at Baños Chavin.

3.2 Analytical techniques

Oxygen, hydrogen, and carbon stable isotope ratios were measured at the Utah State University (USU) Stable Isotope Laboratory by continuous flow-isotope ratio mass spectrometry (CF-IRMS) using a ThermoScientific Delta V Advantage IRMS and Gasbench II. CO_2 equilibration and H_2 equilibration with Pt reduction methods were used to acquire $\delta^{18}O$ and δD values, respectively. Results are reported in per mil (‰) relative to Standard Mean Ocean Water (SMOW) based on internal laboratory standards, calibrated using Vienna Standard Mean Ocean Water (VSMOW) and Vienna Standard Light Antarctic Precipitation (VSLAP). $\delta^{18}O$ and δD uncertainties were ±0.06‰ and ±2.0‰, respectively.

Carbon stable isotope ($\delta^{13}C$) values were measured from dissolved inorganic carbon in spring water samples using a modified phosphoric acid method (Salata et al., 2000). We modified this method by acidifying the water to liberate CO_2, and calibrating using international standards (NBS 19, LSVEC), and the principle of identical treatment. The principle of identical treatment involves making a dissolved DIC standard of $NaHCO_3$, and calibrating it to solid-phase $NaHCO_3$. Results are reported in per mil (‰) relative to the Pee Dee Belemnite (PDB) scale, with an uncertainty of ±0.1‰, determined by repeat analysis of NBS carbonate standards.

All of the newly sampled springs (n = 12) and six of the springs sampled in 2015 were analyzed for chlorine stable isotope ratios (Table A5). Chlorine stable isotope ratios ($\delta^{37}Cl$) were measured by IRMS equipped with a CH_3Clpurification line at the University

of Texas, Austin (Barnes et al., 2009). $\delta^{37}Cl$ values are reported in per mil (‰) relative to Standard Mean Ocean Chlorine (SMOC) based on internal laboratory standards. Analytical precision of $\delta^{37}Cl$ is ±0.2‰, based on long-term analyses of three seawater standards and one rock standard. Dissolved gas compositions were measured at the Volatiles Laboratory, University of New Mexico (UNM) by quadrupole mass spectrometry and gas chromatography.

Major and minor element concentrations were determined at the USU Water Research Laboratory using a Dionex Ion Chromatograph (anions) and Agilent ICP-MS (cations). Geochemist's Workbench (Bethke, 2008) was used to calculate charge balances, saturation indices, and total dissolved solids. Total alkalinity was measured by manual colorimetric titration.

3.3 Geothermometry

Conventional SiO_2, Na-K, Na-K-Ca, and K-Mg geoindicators (geothermometers) were utilized to estimate subsurface reservoir temperatures for each thermal spring. These reservoir temperatures are empirical calculations based on the assumption of water-rock chemical equilibrium at depth, and the preservation of equilibrium during migration to the surface (Fournier, 1977; Giggenbach, 1988). Silica geothermometers are based on the solubility of silica species (i.e. quartz, chalcedony) in water, as a function of temperature and pressure (Fournier, 1977). Thus, silica precipitation along flow paths can cause problems in the confidence of this geothermometer. The quartz geothermometer is best suited for reservoir temperatures >150°C and the chalcedony geothermometer is a better

approximation for temperatures <150°C. The Na-K cation geothermometer is based on the equilibrium between hydrothermal fluids and feldspars, and Na-K-Ca reflects equilibrium for feldspars and calcite (Giggenbach, 1988). The advantage to the Na-K geothermometer is that it re-equilibrates more slowly than the silica geothermometer, and can reveal temperatures from the deepest section of the reservoir (Giggenbach, 1988). The Na-K geothermometer is most applicable to waters with reservoir temperatures >100 °C and minimal Ca ($\log[Ca^{1/2}/Na] + 2.06 < 1$) content (Fournier and Trusdell, 1973). The Na-K-Ca geothermometer is designed for higher concentrations of Ca and assumes the total conversion of Ca-plagioclase to calcite (Fournier and Truesdell, 1973). Unlike the Na-K and Na-K-Ca geothermometers, the K-Mg geothermometer re-equilibrates rapidly at cooler temperatures, thereby preserving a cooler and likely shallower reservoir signal (Giggenbach, 1988). The K-Mg geothermometer is also more influenced by mixing with shallow ground waters containing dissolved Mg. Differences and similarities between geothermometry temperatures can provide valuable information about the circulation depth and degree of fluid-rock interaction in thermal spring fluids.

4. Results

4.1 Aqueous geochemistry

Apparent flow rate and degassing (bubbling at source) varied between springs, and temperature, pH, and conductivity range from 16.9 – 88.9 °C, 5.0 – 7.9, and 170 – 23,000 µS, respectively (Table 1). Major element compositions are highly variable. However, all

Group 1 springs and majority of Group 2 springs exhibit Na-Cl type waters (Fig. 5). In contrast, Group 3 and Group 4 springs display a wide range of water types (Na-HCO_3, Ca-SO_4, Ca-Cl, Na-Cl, Ca-HCO_3) (Fig. 5). Springs from Groups 1 and 2 yielding Na-Cl water types are distinguished by relatively high concentrations of total dissolved solids (TDS) (up to 15,357 mg/l). Groups 3 and 4 yield <1,000 mg/l in TDS (excluding Baños Jocos Peinado; Fig. 6). Group 3 spring, Jocos Peinado yields Ca-SO_4 water, containing 2,814 mg/l in TDS and the highest concentration of SO_4^{2-} (1,452 mg/l) among the 25 spring samples analyzed (Fig. 6).

Table 1. Sample ID, location, and field parameters for hot springs in the Cordillera Blanca and Cordillera Huayhush, Peru.

Group/Location (Baños)	Sample ID	Latitude	Longitude	Elevation (m)	T (°C)	pH	Cond. (uS)
Group 1							
Huancarhuaz	DN13CB11	-8.94365	-77.78461	2721	73.3	6.22	5120
Aquilina	DN13CB14	-8.61294	-77.88359	1930	78.3	6.26	2130
Huancarhuaz	DNCB15-08	-8.9415	-77.7853	2721	69.9	6.4	5750
Pacatque	DNCB15-10	-8.61294	-77.88359	-	88.9	6.84	2280
Group 2							
Olleros 2b	DN13CB05	-9.6683	-77.46262	3453	20.4	6.56	23200
Olleros 4	DN13CB06	-9.6673	-77.46327	3432	47.8	6.49	21500
Merced	DN13CB07	-9.2591	-77.61185	3002	38.4	5.03	723
Chancos	DN13CB08b	-9.31958	-77.57518	2863	47.6	6.22	6020
Monterrey	DN13CB09	-9.46841	-77.53543	2983	46.4	5.89	6240
Shangol	DN13CB13	-8.98458	-77.81697	2214	39.6	6.01	1025
Pumapampa	DNCB15-12	9.880278	77.286389	4185	19.2	5.95	3970
Recuay	DNCB15-13	-9.718	-77.459	-	16.9	6.81	14380
Group 3							
Aticara	DNCB15-11	-8.6125	-77.8836	2662	36.6	8.87	170
Pomabamba	DNCB17-2	-8.826	-77.46	2910	50.5	6.62	468.2
Chihuan	DNCB17-6	-8.672	-77.634	3304	36.5	7.02	606.6
Rupac	DNCB17-9	-8.595	-77.566	2443	61.5	6.18	229.5
Jocos Peinado	DNCB17-13	-8.295	-77.488	1591	40.6	6.31	3332
Chavin	DNCB17-21	-9.611	-77.182	3214	41	7.47	1406
Group 4							
Conococha	DNCB17-24	-10.129	-77.289	4026	28	7.98	233.1
Azulmina	DNCB17-25	-9.938	-76.963	3870	70.7	5.96	1452
Taurimpampa	DNCB17-30	-9.847	-76.817	3244	45.3	6.24	1387
Banos (Batan)	DNCB17-32	-10.048	-76.722	3390	64.7	5.71	940.3
Conoc (La Union)	DNCB17-36	-9.781	-76.805	3175	42.2	6.68	376.7
Machaycancha (Conog)	DNCB17-37	-10.164	-76.811	3835	44.6	6.4	567.6
Janac	DNCB17-38	-10.154	-76.902	4343	51.5	6.48	720.3

- not determined

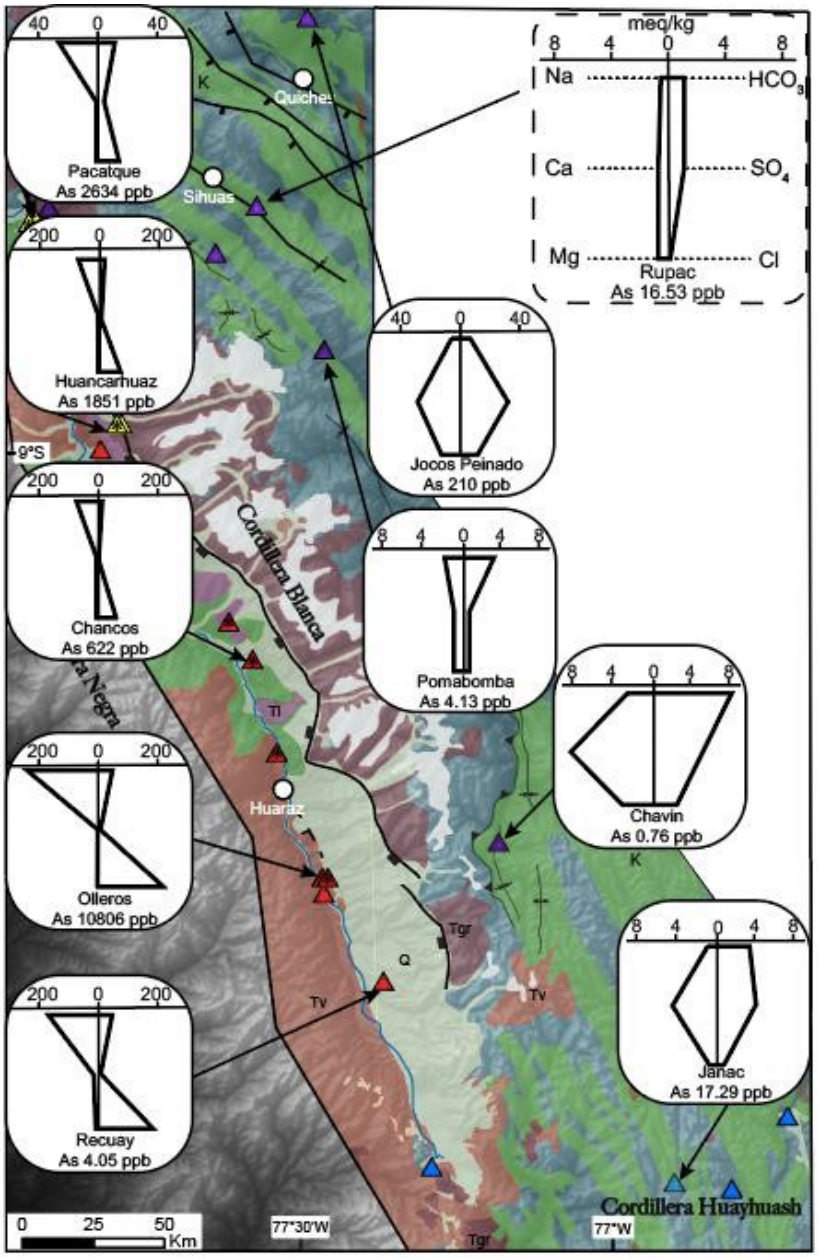

Figure 5. Spatial relation of thermal spring water types as a function of the CBD. Legend (top-right) denotes major element constituents represented by Stiff diagrams. The shape of the Stiff diagrams corresponds to the relative concentration of major elements in each water sample. Springs along the trace and in the hanging-wall of the CBD (left) are characterized as Na-Cl type waters, with concentrations up to 200 meq/kg. Springs in the footwall of the CBD and in the Cordillera Huayhuash (right) exhibit a variety of water types with significantly lower concentrations. Several springs from each group are represented to highlight trends, but not all samples are shown. Arsenic (As) concentrations are also shown for reference.

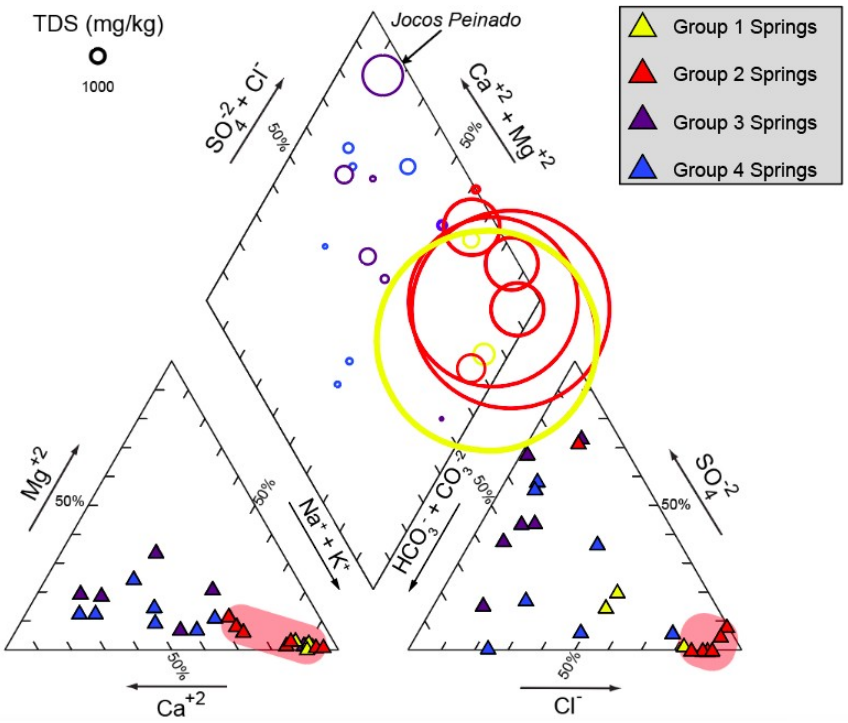

Figure 6. Piper diagram (Piper, 1944) illustrating the major ion chemistry in thermal springs divided into groups based on geographic location. In the middle parallelogram, the total dissolved solids (TDS, mg/kg) are scaled by circle size. Note that the Group 1 and 2 springs are dominated by Na-Cl water types and have muchhigher TDS than Group 3 and 4 springs. Red-shaded areas highlight Na-Cl dominated waters.

Additional halogen data (Br, and $\delta^{37}Cl$) were measured from a subset (n = 18 of 25) of thermal springs to evaluate salinity sources. Spring waters exhibit a range of chloride-bromide (Cl/Br) molar ratios, with Group 1 (626 – 1148) and Group 2 (1038 – 1410) springs generally yielding ratios higher than Group 3 (228 – 1095) and Group 4 (331 – 586) springs (Table A5). This distinction is illustrated in Figure 7A, where Group 1 and 2 springs have ratios higher than seawater and Group 3 and 4 springs contain ratios lower than seawater (excluding Baños Chihuan). Halogen data from thermal springs emanating

along other representative active volcanic arcs (Taupo Volcanic Zone - New Zealand, Bernal et al., 2014; Cascade arc, Cullen et al., 2015), are included for comparison (Fig. 7). Cl/Br ratios from arc-related springs overlap and plot similarly to Cl/Br ratios of Group 1 and 2 springs (Fig 7A). Baños Recuay contains substantially more Cl^- (6019 mg/l) than most springs and plots as a horizontal deviation from other springs in Figures 7B and 7D.

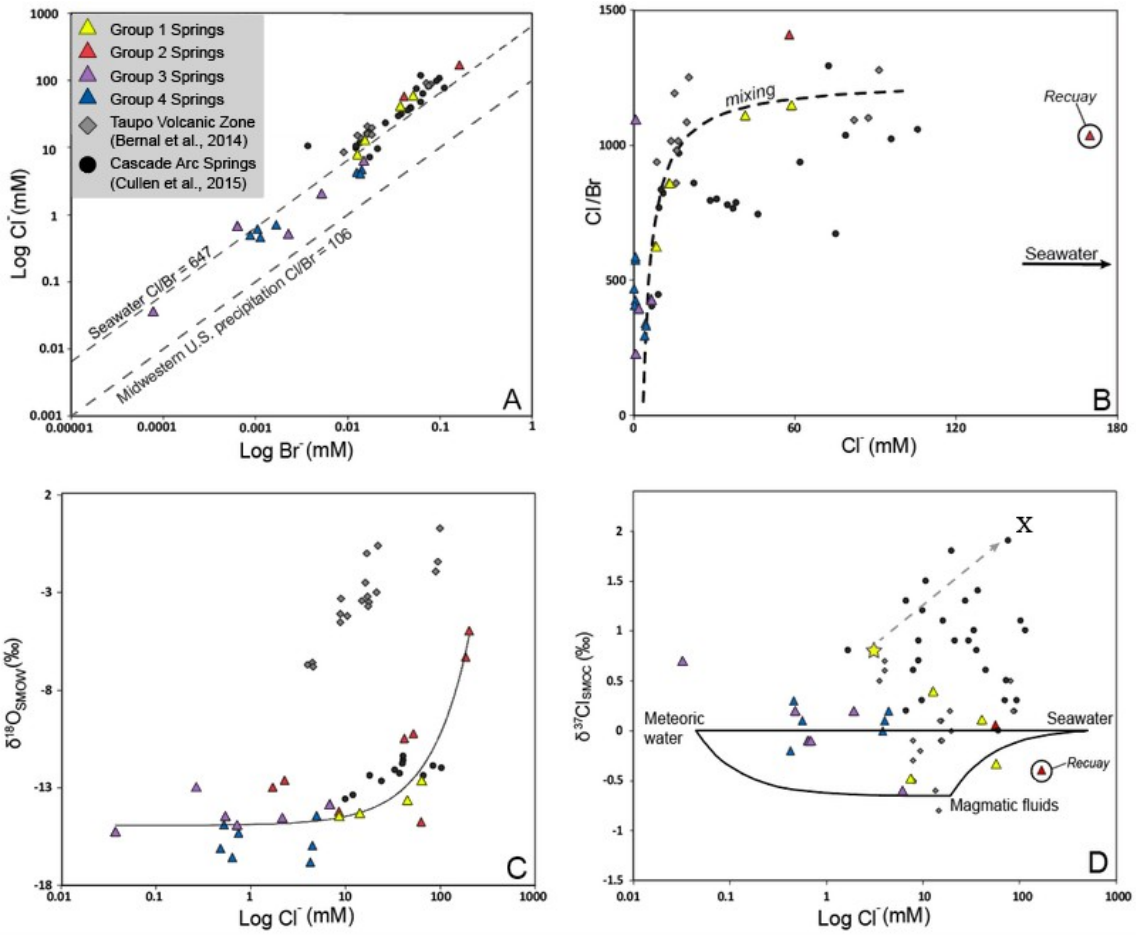

Figure 7. Evaluation of salinity sources in hot springs along the Cordillera Blanca and Huayhuash. Other arc-related systems are shown for reference to aid in interpreting data (Bernal et al., 2014; Cullen et al., 2015). A) Cl^- vs. Br^-, with the molar ratio of seawater (Cullen et al., 2015) and Midwestern U.S. precipitation (Panno et al., 2006) denoted by dashed lines. Group 1 and 2 springs generally exhibit Cl/Br ratios greater than seawater, consistent with other arc-related springs. B) Group 1 springs fall on a mixing trend between a saline and dilute end-member on a plot of Cl/Br vs. Cl^-. Cl^- and Cl/Br end-members that are most sensitive to the data are: 3.5 mM and 50 for dilute water and 100 mM and 1,200 for saline source. We consider Baños Recuay an outlier to the data, with a significantly higher Cl^- concentration, and thus not included in the fit of the mixing trend (see text for discussion). C) Data from this study and arc-related springs exhibit a positive correlation between $\delta^{18}O$ values and Cl^- content. D) Cl-source ternary mixing model (after Li et al., 2015), displaying high variability among Cl sources in data from this study and arc-related springs. Cullen et al., (2015) suggests that basalts (star) in the Cascade Range control $\delta^{37}Cl$ values, but that an additional source or process (X) are required to account for the full range of values.

Trace element concentrations vary between springs, but notable constituents across all groups include aluminum, iron, zinc, antimony, titanium, and arsenic (Table A3). Group 1 and 2 springs generally yield higher concentrations of trace elements than Group 3 and 4 springs (Table. A3). For example, Group 1 springs contain up to 10,800 ppb arsenic (As) and Group 2 springs contain up to 2,600 ppb As; compared to Group 3 (up to 200 ppb As) and Group 4 (up to 600 ppb As) springs. Sr and Ba are positively correlated with Cl^- concentration (Fig. A1).

4.2 Stable isotope geochemistry

New oxygen ($\delta^{18}O$) and hydrogen (δD) stable isotope ratios were acquired from CB and CH hot springs (n = 21, including duplicates), and combined with previously published spring data (n = 9, including duplicates; Table 2; Newell et al., 2015). Investigated hot spring groups range in $\delta^{18}O$ and δD from -14.4 to -12.6 and -113 to -94 ‰ (Group 1), -14.7 to -4.9 and -111 to -74 ‰ (Group 2), -15.3 to -13.1 and -116 to -94 ‰ (Group 3), and -16.8 to -14.4 and -130 to -115 ‰ (Group 4), respectively (Table 2). A majority of springs from Groups 1, 3, and 4 display an affinity to meteoric water and plot along the Global Meteoric Water Line (GMWL) (Fig. 8A). More specifically, Group 4 springs fall contain the lowest values along the GMWL (Fig. 8A). In contrast, Group 2 springs possess $\delta^{18}O$ ratios higher than meteoric water and δD ratios below the GMWL and define a trendline with a slope of 3.1 ($R^2 = 0.87$) (Fig. 8A). Collectively, $\delta^{18}O$ ratios from all investigated hot springs exhibit a positive relationship with increasing Cl^- concentration (Fig. 7C). $\delta^{18}O$ ratios and Cl^- content from arc-related springs show a similar correlation and Cascade-arc

springs overlap with Group 1 and 2 springs from this study (Bernal et al., 2014; Cullen et al., 2015) (Fig. 7C).

We also report $\delta^{18}O$ and δD ratios from streams and ponds (n = 5) representative of local meteoric water. These ratios from local meteoric water are combined with values reported by Newell et al. (2015) and Mark and McKenzie (2007) to assess a general signature of local waters in the CB and CH region (Fig. 8A). Stable isotope ratios from Mark and McKenzie (2007) comprise glaciated and non-glaciated waters strictly from the CB. Note that two samples of meteoric water contain similar $\delta^{18}O$ and δD ratios as springs in Group 2 (Fig 8A). One of these samples is sourced from a small pond (~3 m in diameter) near the town of Quiches (this study), and the other is sourced from a highly evaporitic lake (Lake Conococha), near the town of Conococha (Mark and McKenzie, 2007) (Fig. 2).

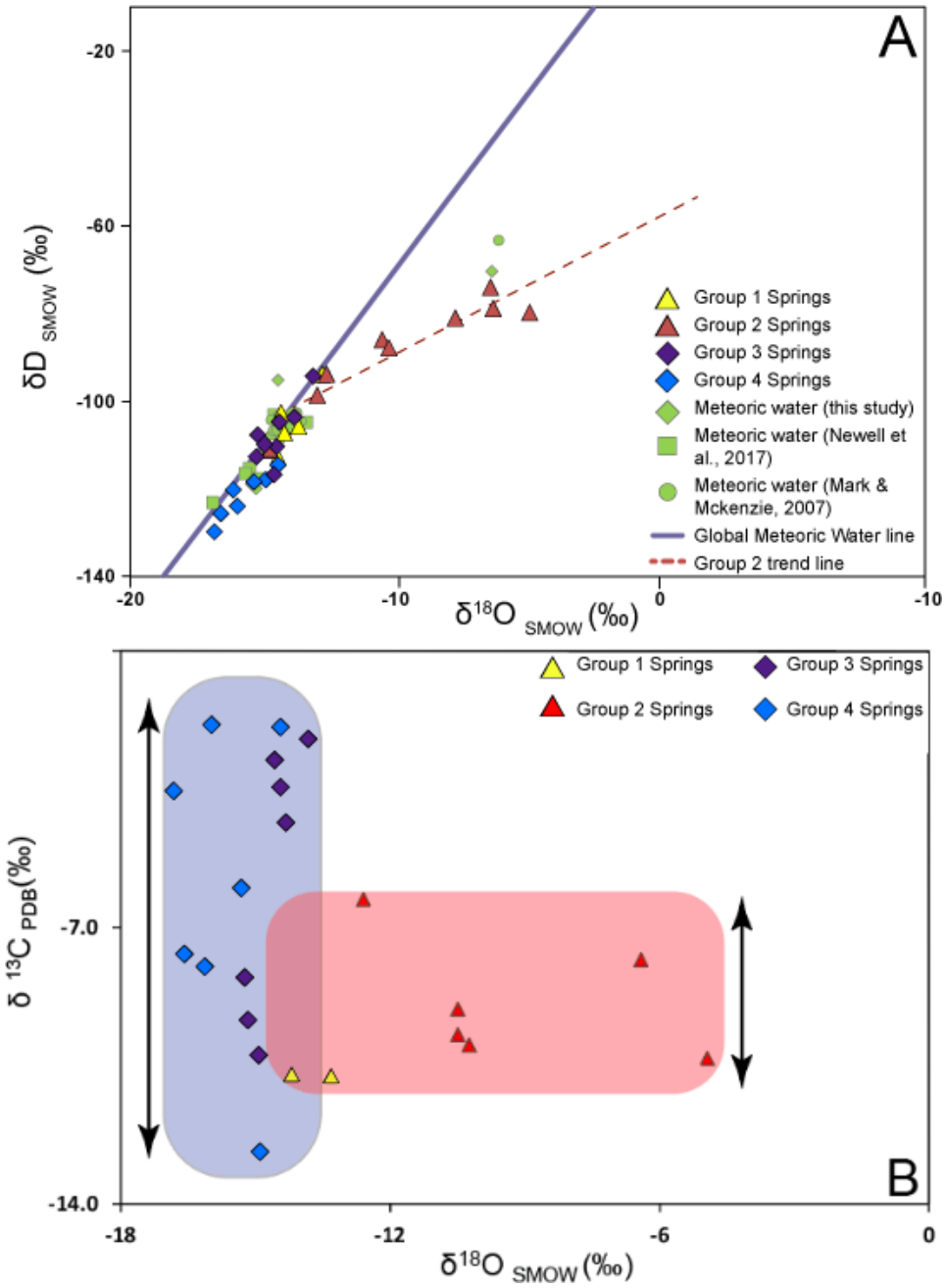

Figure 8. A) $\delta^{18}O$ versus δD for thermal springs and cold local meteoric water in the Cordillera Blanca region. Group 2 springs form a linear trend to values higher than local meteoric water and Group 1, 3, and 4 springs fall along the GMWL. B) $\delta^{13}C$ (dissolved inorganic carbon) and $\delta^{18}O$ of springs in the Cordillera Blanca and Huauyhuash. Disparities in the range of $\delta^{13}C$ and $\delta^{18}O$ between springs groups are highlighted.

Carbon ($\delta^{13}C$) stable isotope ratios in dissolved inorganic carbon were measured from a subset (n = 22 of 30) of thermal spring water samples (Table 2). Groups 1 and 2 exhibit a distinct relationship in their $\delta^{13}C$ vs. $\delta^{18}O$ ratios, compared to Groups 3 and 4. Group 1 and 2 springs yield a relatively narrow range in $\delta^{13}C$ ratios (-10.8 to -6.3 ‰) and wide range in $\delta^{18}O$ ratios (-14.7 to -4.9), compared to Group 3 and 4 springs that yield a wider range in $\delta^{13}C$ ratios (-12.6 to -1.8 ‰) and narrower range in $\delta^{18}O$ ratios (-16.8 to -13.8) (Fig 8B; Table 2).

We report chlorine ($\delta^{37}Cl$) stable isotope ratios from a subset (n = 18 of 30) of spring samples that range from -0.6 to 0.7 ‰ (Table 2), exhibiting no apparent trends with geographic location (spring groups). There are also no significant correlations between $\delta^{37}Cl$ ratios and temperature, Cl^- concentrations, or $\delta^{18}O$ values (Fig. A2). $\delta^{37}Cl$ and Cl^- data from this study are compared to a Cl-source ternary mixing model (Li et al., 2015), alongside similar data from arc-related hot springs (Taupo Volcanic Zone - New Zealand, Bernal et al., 2014; Cascade arc, Cullen et al., 2015) (Fig. 7D). We observe some variability in our $\delta^{37}Cl$ data; however, springs from comparative studies show similar to even more variability (Fig. 7D).

Table 2: Stable isotope ratios (O, H, C, Cl) measured from springs in the CB and CH ranges.

Thermal Spring (Baños)	**Sample ID**	**Elevation (m asl)**	**$\delta^{18}O$ (‰) SMOW**	**δD (‰) SMOW**	**$\delta^{13}C$ (‰) PDB**	**$\delta^{37}Cl$ (‰) SMOC**
Group 1						
Aquilina	DN13CB14	1930	-14.2	-107.3	-10.7	-
Huancarhuaz	DNCB15-7	-	-13.6	-105.9	-10.8	0.1
Huancarhuaz	DNCB15-8	2721	-12.6	-94.4	-	-0.3
Aqulina	DNCB15-9b	1884	-14.4	-112.9	-	-0.5
Pacatque	DNCB15-10	-	-14.3	-102.6	-	0.4
Group 2						
Olleros 1	DN13CB04	3464	-7.8	-81.1	-	-
Olleros 2b	DN13CB05	3453	-6.4	-74.3	-7.8	-
Olleros 4	DN13CB06	3432	-4.9	-79.8	-10.3	-
Merced	DN13CB07	3002	-12.6	-94.4	-6.3	-
Chancos	DN13CB08a	2863	-	-	-9.0	-
Chancos	DN13CB08b	2863	-10.5	-85.9	-9.7	-
Monterrey	DN13CB09	2983	-10.2	-87.7	-10.0	-
Shangol	DN13CB13	2214	-13.0	-98.5	-	-
Pumapampa	DNCB15-12	4185	-14.7	-111.0	-	0.1
Recuay	DNCB15-13	-	-6.3	-78.8	-	-0.4
Group 3						
Aticara	DNCB15-11	2662	-13.1	-93.9	-	-
Pomabamba	DNCB17-1	2901	-14.3	-104.2	-4.3	-
Pomabamba	DNCB17-2	2910	-14.5	-110.1	-3.4	0.2
Chilhuan	DNCB17-6	3304	-14.9	-109.7	-10.2	-0.1
Rupac	DNCB17-7b	2360	-15.2	-107.3	-9.3	-
Rupac	DNCB17-9	2443	-15.3	-112.6	-8.2	0.7
Jocos Peinado	DNCB17-13	1591	-13.8	-103.3	-2.2	-0.6
Chavin	DNCB17-21	3214	-14.6	-116.1	-2.7	0.2
Group 4						
Conococha	DNCB17-24	4026	-14.9	-117.8	-12.6	0.3
Azulmina	DNCB17-25	3870	-16.0	-123.9	-1.8	0.1
Taurimpampa	DNCB17-30	3244	-14.4	-114.5	-1.9	0.2
Banos (Batan)	DNCB17-32	3390	-16.8	-129.9	-3.5	0
Conoc (La Union)	DNCB17-36	3175	-15.3	-118.2	-6.0	-0.1
Machaycancha	DNCB17-37	3835	-16.1	-120.3	-8.0	-0.2
Janac	DNCB17-38	4343	-16.6	-125.4	-7.7	0.1

-not determined

4.3 Gas geochemistry

Dissolved gas compositions (water vapor free) in water samples from a subset (n = 11 of 25) of hot spring samples are reported in Table A6. Major volatile compositions are dominated by CO_2 (17 – 96 mol %) and N_2 (3 – 87 mol %). We also observe lesser amounts of O_2 (< 4 mol %), Ar (< 2 mol %), CH_4 (<1.5 mol %), He (<0.5 mol %), H_2 (<0.2 mol %), and CO (<0.01 mol %). Hot spring samples fall on a mixing line between a mantle/crust origin and meteoric end-member (Fig. 9). Two Group 3 springs, Rupac and Jocos Peinado, contain undetectable amounts of dissolved He, and therefore plot on the Ar – N_2 tie line (Fig. 9). In order to quantify the mantle versus crustal contributions, additional isotopic data are required, such as $^3He/^4He$ ratios.

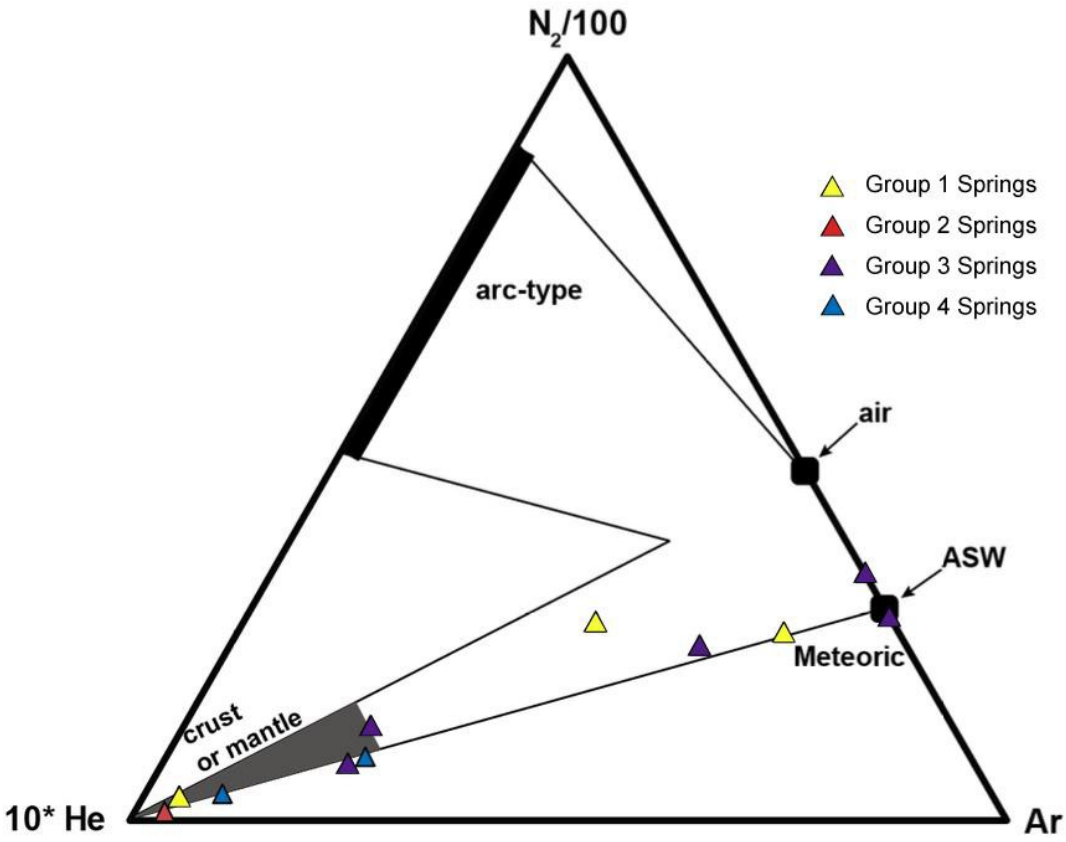

Figure 9. Inert gas ternary diagram, depicting relative abundance of He, N_2, and Ar (after Giggenbach, 1992). Air and air-saturated water (ASW) are plotted for reference. Gases from investigated hot springs primarily fall along a mixing line between crust/mantle and meteoric water.

4.4 Geothermometry

Reservoir temperatures from a subset (n = 23 of 25) of CB and CH hot springs are estimated using silica and various cation geothermometers (Fournier and Truesdell, 1973; Fournier, 1977; Arnorsson et al., 1983; Giggenbach, 1988). Several distinctions between geothermometers are observed across all spring groups. Springs, excluding Baños Huancarhuaz, yield quartz geothermometer temperatures <150 °C, making the chalcedony geothermometer more applicable (Fournier, 1977) (Table 3). Hot spring temperatures

provided by the chalcedony geothermometer (36 – 141 °C) are relatively lower than their corresponding Na-K (120 – 351 °C) and Na-K-Ca (40 – 245 °C) geothermometry temperatures (Table. 3). Note that dissolved silica was not measured on the 2015 samples, and thus silica temperatures are not calculated for these 5 springs (Table 3). The majority of reservoir temperatures provided by the K-Mg geothermometer (44 – 172 °C) are also lower than corresponding Na-K and Na-K-Ca temperature estimates (Table. 3).

Reservoir temperature estimates are also observed to vary between spring groups. Surface temperatures from all Group 1 springs (73 – 89 °C) are notably higher than Group 2 (17 – 48 °C), Group 3 (37 – 62 °C), and Group 4 (28 - 71 °C) springs (Table 3). Reservoir temperatures calculated using the Na-K-Ca geothermometer are generally higher in Group 1 (152 - 226 °C) and Group 2 (91 – 245 °C) springs, than in Group 3 (42 – 79 °C) and Group 4 (40 – 98 °C) springs (Table 3). This relationship is also exhibited by temperatures calculated with the K-Mg geothermometer: Group 1 (121 – 167 °C) and Group 2 (71 – 172 °C), versus Group 3 (45 – 65 °C) and Group 4 (44 – 77 °C) (Table 3).

A ternary comparing Na-K and K-Mg geothermometers (Giggenbach, 1988), shows that several Group 1 and 2 springs plot in the “partial equilibrium field”, yielding Na-K temperatures from 200 – 275 °C and K-Mg temperatures from 71 – 172 °C (Fig. 10). All of the Group 3 and 4 springs plot as “immature waters” with unreliable reservoir temperatures and proportionally higher amounts of dissolved Mg (Fig. 10). Additionally, four springs from Groups 3 and 4, Baños (Rupac, Conoc, Machayacancha, and Janac), yield Na-K-Ca temperatures that are lower than their corresponding surface temperature

(Table 3). We observe this same contradicting relationship from the chalcedony geothermometer (Jocos Peinado, Chavin, Batan) and K-Mg geothermometer (Rupac, Azulmina), strictly among the Group 3 and 4 springs (Table 3). Reservoir temperature estimates that are erroneously low is a common result of thermal fluid disequilibrium from a meteoric influence (Yock, 2009; Karingithi, 2009).

Table 3. Reservoir temperatures calculated using silica and cation geothermometers.

Thermal Springs (Baños)	**Surface Temp (°C)**	**Quartz conductive (Fournier, 1977)**	**Chalcedony conductive (Arnorsson et al., 1983)**	**Na-K (Giggenbach, 1988)**	**Na-K-Ca (Fournier and Truesdell, 1973)**	**K-Mg (Giggenbach, 1988)**
Group 1						
Huanacarhuaz	73.3	169	141	260	226	167
Aquilina	78.3	140	112	200	152	121
Pacatque	88.9	-	-	220	168	132
Group 2						
Olleros	47.8	-	-	265	245	172
Merced	38.4	85	57	263	91	71
Chancos	47.6	140	112	275	209	137
Monterrey	46.4	-	-	257	229	147
Shangol	39.6	87	58	234	108	83
Pumapampa	19.2	-	-	313	176	118
Recuay	16.9	-	-	242	217	136
Group 3						
Aticara	36.6	-	-	120	43	55
Pomabamba	50.5	113	84	273	79	58
Chihuan	36.5	89	60	189	44	50
Rupac	61.5	101	73	348	48	45
Jocos Peinado	40.6	67	38	326	66	65
Chavin	41	65	36	248	42	46
Group 4						
Conococha	28	67	38	226	44	51
Azulmina	70.7	110	81	285	78	69
Tauripampa	45.3	106	77	288	80	76
Baños Batan	64.7	91	62	284	98	77
Conoc	42.2	78	49	294	42	44
Machayacancha	44.6	98	69	333	43	57
Janac	51.5	127	99	351	40	56

- not determined

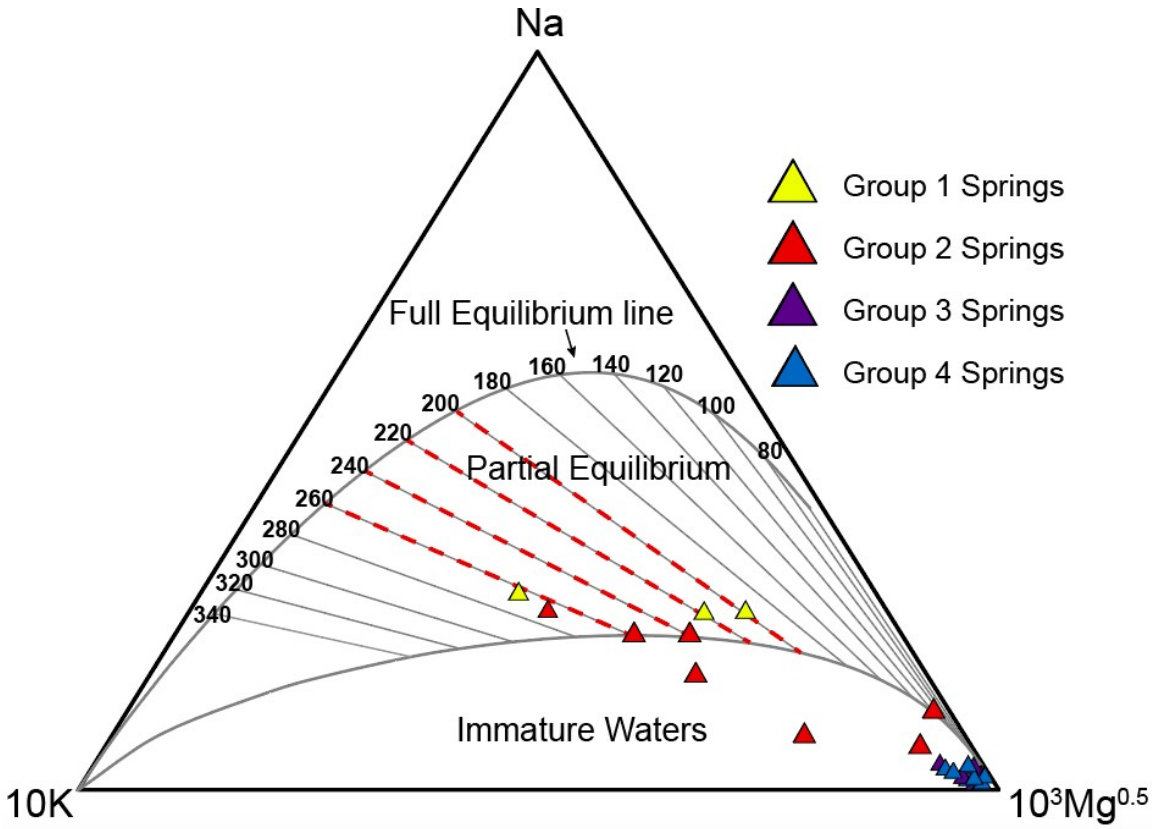

Figure 10. Geothermometry ternary diagram of the Na-K and K-Mg geothermometers (modified from Giggenbach, 1988). Group 3 and 4 springs plot as immature waters in the Mg corner and Group 1 and 2 springs exhibit a range of trends, including along the 200-260°C Na-K isotherms in the partial equilibrium field.

5. Discussion

Aqueous and stable isotope geochemistry data are compared from spring groups (1 – 4) to discern the role of structures like the CBD as a conduit for deeply circulated fluids. Thermal springs located along the hanging-wall of the CBD (Group 2) are interpreted to

issue from steep normal faults that intersect with the CBD at depth (Newell et al., 2015). Compared to Groups 3 and 4 springs, Groups 1 and 2 springs both yield predominantly Na-Cl water types, high TDS, elevated trace metals, similar stable isotope geochemistry, and a higher range of calculated geothermometry temperatures. Geochemical and stable isotope similarities between Group 1 and Group 2 springs support an interconnected fracture network promoting deep fluid pathways for these two groups. Data from Groups 1 and 2 also suggest mixing with hydrothermal brine at depth, facilitated by these interrelated flow-paths (Fig. 11). In contrast, data from Groups 3 and 4 springs lack evidence for deep brine influence, and reflect shallower circulation and equilibration with the sedimentary host rock. This study reveals that the CBD and adjoining normal faults promote deep fluid migration, thereby affecting fluid-rock interactions and resulting fluid geochemistry. Moreover, these results reveal a fault-controlled mechanism for deeply-derived mantle volatiles measured in hot springs to migrate through the brittle crust (e.g., Kennedy et al., 1997; Mutlu et al., 2008; Newell et al., 2015).

5.1 Geochemistry of Group 1 and Group 2 springs

Group 1 and Group 2 springs are both dominated by Na-Cl water types with TDS concentrations up to 15,357 mg/l (Figs. 5, 6). These data suggest relatively high TDS, Na-Cl rich source, and/or fluid-rock reactions controlling their water chemistry. Na-Cl water types can result from meteoric recharge mixing with deeply sourced hydrothermal brine, similar to processes observed at active volcanic arcs (Fournier, 1987, Giggenbach et al., 1990). Volatiles derived from emplaced magma can produce brine; however, we currently

lack evidence of active magmatism in this setting. Alternatively, fluid interaction with sodic plagioclase (albite) and alteration minerals (e.g., chlorite) can yield a Na-Cl brine characteristic of deeply circulating fluids in a granite reservoir (Kuhn, 2004; Bucher and Stober, 2010; Pepin et al., 2014). Possible origins for Cl^- in this setting include residual Cl-rich fluids partitioned from earlier magmatism (~5 Ma) and/or prolonged circulation of dilute fluids through hot rocks with a history of magma injections (Fournier, 1987).

Leaching of evaporites in host rocks along the flow-paths may also explain the Na-Cl dominated waters. Cl/Br molar ratios are informative as a geochemical tracer for sources of chloride, and thus salinity in crustal fluids (Kesler et al., 1996; Panno et al., 2006; Leisen et al., 2012; Bernal et al., 2014). Hydrothermal leaching of evaporite would result in Cl/Br ratios that are substantially higher than seawater (647). Br^- does not substitute into halite, so dissolution of halite typically results in Cl/Br ratios >10,000 (Banks et al., 2000; Leisen et al., 2012). Cl/Br ratios from Group 1 and 2 springs are only ~2X the ratio of seawater (Fig. 7A), implying evaporite dissolution is not the dominant source of chloride. This is consistent with the lack of reported evaporite units in the sedimentary rock-types, and supradetachment basin-fill sediments along the CBD (Giovanni et al., 2010).

Serpentinites, formed by the hydration of the mantle lithosphere, are a potential source of Cl^- (0.2 -0.5 wt%) in subduction zones (Sharp and Barnes, 2004; Kendrick et al., 2011). Dehydration of a subducting flat slab and transfer of Cl-rich fluids to the lithosphere may lend to the observed Na-Cl water types (Humphreys et al., 2003; Hoke and Lamb, 2007; Butcher et al., 2017). This process may not sufficiently account for the localized

distribution of Na-Cl springs along the trace and hanging-wall of the CBD; however, it should not be ruled out as a possibility.

$\delta^{18}O$ and δD stable isotope ratios are useful for discerning fluid phase changes, fluid-rock interactions, and/or fluid mixing (Sharp, 2007). Unlike Group 1 springs that exhibit an affinity to meteoric water, Group 2 springs contain $\delta^{18}O$ and δD ratios that deviate from the GMWL (Fig. 8A). This deviation in $\delta^{18}O$ and δD ratios is likely the result of mixing between groundwater and a brine that has exchanged at elevated temperatures with silicate bedrock (see Newell et al., 2015). Contributions from brine is also consistent with high concentrations of TDS and trends in major element concentrations (Fig. 6)

Trends observed in halogen data (Cl^-, Cl/Br, $\delta^{37}Cl$) from this study support mixing between different brine and groundwater sources (Fig. 7B). Several studies use halogen data to assess mixing between groundwater and higher-salinity sources (e.g., seawater, brine, halite, magmatic fluids; Katz et al., 2011; Leisen et al., 2012; Li et al., 2015). Following this approach, Fig. 7B shows that a binary mixing line between a dilute meteoric end-member and a Cl-rich source explain most of our data. Baños Recuay contains significantly more Cl^- (6019 mg/l) than other springs in the region and deviates horizontally from the Cl/Br vs. Cl^- mixing trend (Fig. 7B). Waters emanating from Recuay were observed to have particularly low discharge, potentially resulting in increased evaporation and therefore increased Cl^- concentrations. Specifically, evaporative concentration below halite saturation will not change the Cl/Br ratio but will increase the Cl^- content (Katz et al., 2011), resulting in the horizontal shift on Figure 7B. Similarly, this evaporative

concentration at Recuay results in an increase in Cl^- without altering $\delta^{37}C$ values (Fig. 7D). Baños Recuay is therefore excluded from the fit of the mixing trend due to likely evaporative processes occurring at the surface.

The broad range in $\delta^{37}Cl$ values supports our interpretation of mixing between dilute and brine-like fluid sources (Fig. 7D). $\delta^{37}Cl$ is a powerful provenance tool used for accessing the contribution and mixing of different chlorine sources (e.g., mantle, seawater, subducted marine sediments, volcanic rocks at depth) (Chiaradia, et al., 2014; Cullen et al., 2015). Our data is consistent with the spread of $\delta^{37}Cl$ values observed at arc-related hot springs (Bernal et al., 2014; Cullen et al., 2015), and could indicate a mixture between a "seawater" source and a deeper crustal (or magmatic) end member, diluted by meteoric water (Fig. 7D). Cullen et al. (2015) attributes high $\delta^{37}Cl$ values and Cl^- concentrations to fluid-rock interactions with volcanic rocks at depth (Fig 7D). They recognize that volcanic rocks cannot account for the full range of values and suggest that additional mechanisms, such as contribution from ^{37}Cl-enriched HCl vapor via magmatic degassing, are required (Fig. 7D).

Aqueous and stable isotope geochemistry data from Group 1 and 2 springs support mixing between a localized Cl-rich source and groundwater. We propose that hydrothermal brine is located at depth and focused within the hanging-wall of the CBD, thereby only contributing to Group 1 and Group 2 springs (Fig. 11). We favor mixing between meteoric recharge and brine as a plausible origin for the high TDS, Na-Cl dominated waters with higher-than-meteoric $\delta\ ^{18}O$ and δD values.

5.2 Geochemistry of Group 3 and Group 4 springs

In contrast to Group 1 and Group 2 springs, Group 3 and Group 4 springs exhibit a wide range of water types with relatively low TDS (<1000 mg/l) (Figs. 5, 6). This suggests that these springs do not share a common fluid-rock interaction history, and rather act as separate emanations with individual fluid properties. This is expected because these springs issue from a diverse range of localities: Group 3 – east and northeast of CBD, Group 4 – south of CB and along the CH (Fig. 2). Mixing trends established from Cl/Br ratios and Cl^- concentrations suggest that Group 3 and 4 springs are strongly influenced by dilute meteoric water, likely explaining the overall low TDS measured (Fig. 7B). Dilution of thermal waters in Groups 3 and 4 can also explain geothermometry temperatures that are estimated to be lower than corresponding surface temperatures (Table 3), as well as falling in the "immature water field" of the Giggenbach diagram (Fig. 10). Cl/Br ratios from springs in Groups 3 and 4 are generally lower than the ratio for seawater, unlike Cl- rich springs in Groups 1 and 2 that yield ratios higher than seawater (Fig. 7A). These lower Cl/Br ratios suggest that Group 3 and 4 springs are less influenced by brine at depth and are more indicative of a meteoric signature.

Stable isotope data measured from Group 3 and 4 spring waters also support the influence of local meteoric water. $\delta^{18}O$ and δD values from Group 3 springs are slightly higher than Group 4 springs, but values from both Groups 3 and 4 are notably similar to global meteoric water (Fig. 8A). These low, meteoric-like values from Group 3 and 4 springs typically result from mixing with shallow groundwater and recharge from high

elevation sources. The relationship between low $\delta^{18}O$ and higher altitudes are commonly linked to isotopic fractionation at lower temperatures of precipitation (Dansgaard, 1964; McKenzie et al., 2001). Most Group 4 springs issue from a higher elevation than Group 3 springs, likely explaining the comparably lower $\delta^{18}O$ and δD values (Table 1). The altitude effect is also often mimicked by shallow groundwater, depending on residence time and fluid pathways. Fig. 8A also shows that majority of meteoric samples yield ratios similar to global meteoric water, excluding two samples collected from highly evaporitic settings. Continuous surface evaporation, with a lack of recharge, often results in waters with higher $\delta^{18}O$ and δD values (Dansgaard, 1964), likely explaining the deviation in these two meteoric samples (Fig. 8A).

Collectively, these data indicate that thermal ground waters emanating from Group 3 and 4 springs are geochemically distinct from thermal waters observed at Group 1 and 2 springs. These dilute thermal waters with lower Cl/Br ratios and meteoric-like stable isotope data (Groups 3 and 4) support a dominant shallowly-circulated groundwater influence. Aside from slightly higher $\delta^{18}O$ and δD values in Group 3 springs (Fig. 8A), no apparent trends emerge between Group 3 and Group 4 springs. Baños Jocos Peinado is the one spring that acts as an outlier to the Group 3 springs, yielding 2,814 mg/l in TDS and the highest overall concentration of SO_4^{2-} (1,452 mg/l) (Fig. 6; Table A2). Jocos Peinado also yields the highest As (210 ppb) and lowest $\delta^{37}Cl$ (-0.6) ratio among the Group 3 springs (Table A3, Table 2). This spring emanates from the northeast CB region, where extensional faulting is reported to have triggered a 6.8 Mw earthquake (Quiches fault; Doser, 1987;

Bellier et al., 1991). Pleistocene extension in the northeast CB is hypothesized to be the result of reactivated Eocene thrusts (Bellier et al., 1991). We suggest that Pleistocene extensional features in this region play a role in influencing flow-paths and fluid properties, similar to processes hypothesized for Group 1 and 2 springs.

5.3 Geothermometry and fluid depths

Reservoir temperature estimates (RTE) provided by geothermometry are useful for evaluating temperatures at depth, fluid-rock interaction along flow-paths, and estimates of fluid circulation depth. Processes such as boiling, mineral precipitation during ascent, re-equilibration with rocks along flow-paths, and mixing with shallowly circulated meteoric waters can promote disequilibrium and alter/overprint RTE (Fournier and Truesdell, 1973; Fournier, 1977; Giggenbach, 1988; Yock, 2009). We suggest the Na-K-Ca geothermometry data are most reliable for detecting the deepest fluid circulation depths. The chalcedony geothermometer is susceptible to disequilibrium by silica precipitation during fluid ascent. The loss of dissolved silica to precipitation results in anomalously low RTE (Fournier, 1977). Quartz saturation indices (log SI) for all spring waters fall between 0 and 1 (saturated - supersaturated; Table A2), likely explaining why chalcedony (and most quartz) RTE are lower than the corresponding cation RTE (Table 3). RTE from the Na-K geothermometer are commonly influenced by dissolved Ca, and are applicable when "$\log[Ca^{1/2}/Na] + 2.06 < 1$" (Fournier and Trusdell, 1973). Baños (Olleros, Monterrey, Huanacarhuaz, and Recuay) are the only springs that meet the criteria for the Na-K

geothermometer (Table 3). All other springs in the CB and CH contain relatively high Ca ($\log[Ca^{1/2}/Na] + 2.06 > 1$), making the Na-K-Ca geothermometer ideal for this study.

Geothermometry data provide a means for explaining the geochemical differences between springs along the trace and hanging-wall of the CBD (Groups 1 and 2) and springs east of the CBD and in the CH (Groups 3 and 4). Assuming a geothermal gradient of 25°C/km and an average surface temperature of 0° C, RTE (Na-K-Ca) from Group 1 springs (152 – 226 °C) and Group 2 springs (91 – 245 °C) correspond to circulation depths that range from 6 to 9 km and 4 to 10 km, respectively. In contrast, RTE from Group 3 springs (42 – 79 °C) and Group 4 springs (40 – 98 °C) correspond to substantially lower circulation depths (< 4 km) (Table 3). Geothermometry data from Group 3 and 4 springs also indicate significant disequilibrium between the Na-K and K-Mg geothermometers, denoting these springs as immature waters with proportionally higher dissolved Mg (Fig. 10). At shallow depths, during upwelling and cooling, the K-Mg geothermometer re-equilibrates with host-rock faster than the Na-K system, making disequilibrium common among shallowly circulating fluids at cooler temperatures (Giggenbach, 1988). Dilution from near-surface waters can also promote disequilibrium and might contribute to our observed results. A recent study analyzing hot springs in West Malaysia linked immature waters and disagreement between geothermometers to mixing with near-surface cold water (Baioumy et al., 2015).

We propose that waters emanating from Group 3 and 4 springs are shallowly circulating, compared to the deeper flow-paths interpreted for Group 1 and 2 springs. Additionally, if

fluids from Group 3 and 4 springs have a prolonged residence time in the shallow crust, then they are also likely subjected to mixing with near-surface waters. The distinction in geothermometry temperatures calculated for Groups 1 and 2, versus Groups 3 and 4 could potentially be linked to the presence of Tertiary granodiorite along the flow-paths of Groups 1 and 2, and the relative lack thereof for Groups 3 and 4. However, Baños Aticara (Group 3) and Baños Conococha (Group 4) are two springs that overlie the granodiorite body and yield relatively low geothermometry temperatures, challenging this hypothesis. Also note that these two springs are not located along faults associated with the CBD, similar to most Group 3 and 4 springs (Fig. 2). Differences in circulation depths between Groups 1 and 2 (up to 10 km) and Groups 3 and 4 (up to 4 km) is likely related to the presence and communication within deep fracture networks, such as the CBD and adjoining hanging-wall normal faults. The focusing of thermal fluids along a fault system also likely decreases the amount of mixing with near-surface waters. Although there are some local structures (e.g. thrust faults) associated with Group 3 and 4 springs (Fig. 2), this study suggests that they are not as deeply penetrating as the CBD fracture network. Thus, the difference in flow-paths and fluid-rock interactions that occur along these different paths likely explains the geochemical distinctions between springs in Groups 1 and 2 and springs in Groups 3 and 4.

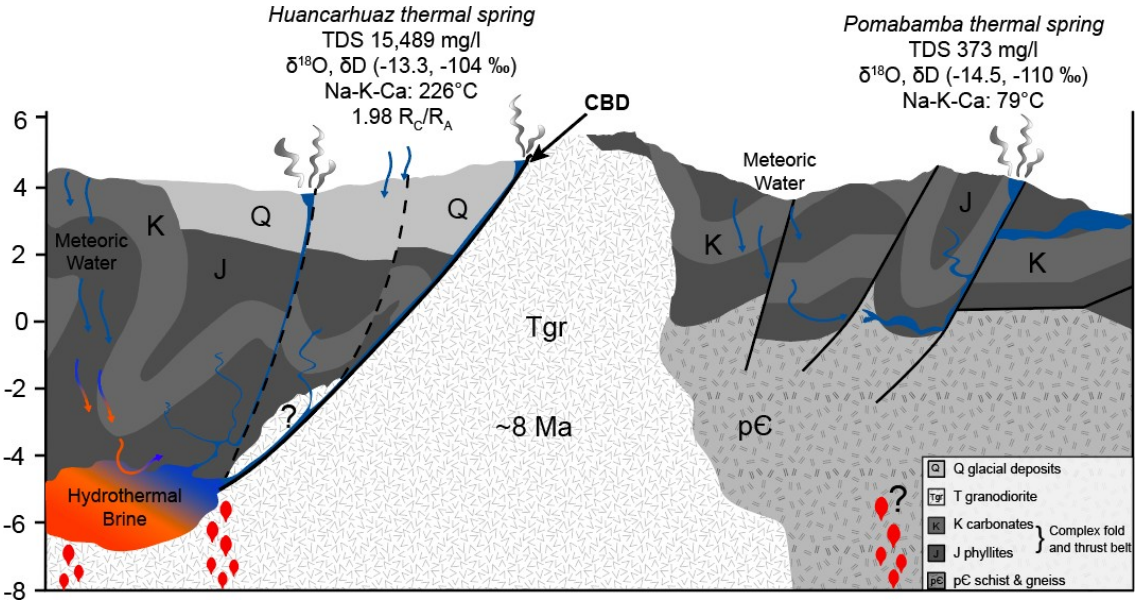

Figure 11. Schematic cross-section through the Cordillera Blanca detachment fault (CBD). Cross-section highlights hypothesized fluid sources and circulation differences between springs east of the CBD (left) and springs west of the CBD (right). Reservoir temperature estimates (Na-K-Ca) and aqueous/stable isotope geochemistry from hot springs are shown for reference. Unknown presence of hanging-wall granodiorite and unknown contribution of mantle volatiles to Group 3 and 4 springs are denoted by (?).

5.4 Fault-controlled fluid chemistry

Aqueous geochemistry and stable isotope data from this study collectively show that deeply-penetrating faults like the CBD impart a significant influence on fluid distribution. We suggest that the CBD acts as a conduit, facilitating deep fluid circulation and the transfer of Na-Cl brine to springs in Groups 1 and 2 (Fig. 11). The 200-km long detachment fault and adjoining hanging-wall normal faults provide a network of preferential flow-paths for vertical fluid flow (including infiltration and advection from depth). Away from the CBD and its hanging-wall, geochemistry and geothermometry data suggest waters emanating from Group 3 and 4 springs do not penetrate as deeply as Group

1 and 2 springs, and therefore reflect a shallower circulation path. For Group 1 and 2 springs, geothermometry suggests fault-controlled fluid circulation to depths up to ~10 km, which is consistent with observations at other major detachment fault zones worldwide. For example, δD of synkinematic micas along the Columbia River detachment in North America (Person et al., 2007) and the central Menderes Massif in western Turkey (Hetzel et al., 2013) indicate meteoric infiltration depths of up to 7 and 8 km, respectively. Meteoric-like δD values from micas along the southern Tibetan detachment in the Himalayas support the penetration of surface waters to depths beneath the brittle-ductile transition zone (Gébelin et al., 2017). These prior investigations conclude that detachment faults provide effective pathways for deep meteoric fluid circulation.

The distinction in flow-paths between springs in Groups 1 and 2, versus springs in Groups 3 and 4 is accompanied by disparate fluid-rock interaction histories, as suggested by the spring geochemistry. Several geothermal studies utilize carbon ($\delta^{13}C$) stable isotopes to discern between organic, carbonate, and mantle derived sources of carbon in fluids (Sano and Marty, 1995; Mutlu et al., 2008; Kulongoski et al., 2013; Newell et al., 2015). $\delta^{13}C$ (CO_2) values typically range from −9 to −4‰ in the mantle, −40 to −20‰ in organic sediments, and −2 to 2‰ in carbonates (Sano and Marty, 1995). In our study area, Group 1 and 2 springs yield a narrow range of relatively low values (-10.8 to -6.3 ‰), consistent with a carbon source dominated by a mix of organic and mantle/crustal carbon (Fig 8B, Table 2). Group 3 and 4 springs springs yield a much wider range of $\delta^{13}C$ values (-12.6 to -1.8 ‰), with higher values suggesting mixing of marine carbonate-derived carbon and

organic carbon (Fig 8B, Table 2). We interpret carbon input differences in this setting to be the result of dissimilar fluid-rock interactions along the flow-paths. If waters emanating from Group 3 and 4 springs are indeed shallowly circulating, then the observed $\delta^{13}C$ values can be explained by fluid-rock interactions with Cretaceous carbonates and organic-rich Jurassic phyllites (Fig. 2). Similar $\delta^{13}C$ values (-4.3 to -1.0 ‰) from normal fault-controlled hot springs in the Tibetan Plateau are interpreted to result from fluid-rock interactions with underlying marine carbonates (Yokoyama et al., 1999). In contrast, $\delta^{13}C$ of deeply circulating waters emanating from Group 1 and 2 springs are less influenced by shallow carbonate bedrock, and instead likely reflect a deep crustal (potentially mantle) source. This notion is supported by elevated $^{3}He/^{4}He$ ratios (up to 25 % mantle-derived) measured in a subset (n = 6 of 10) of Group 1 and 2 springs, indicating contribution from deeply- derived fluids (Newell et al., 2015). The focusing of thermal fluids to the surface along the CBD also likely contributes to the lack of carbonate-like $\delta^{13}C$ ratios in Group 1 and 2 springs.

We also attribute higher trace metal concentrations, specifically As, in Group 1 (up to 10,800 ppb) and Group 2 (up to 2,600 ppb) springs, compared to Group 3 (200 ppb) and Group 4 (up to 600 ppb) springs to differences in fluid-rock interactions (Table A3). The source of As in this region is currently unknown; however, there appears to be a correlation between proximity to the CBD and higher As content. Anthropogenic sources, such as mine drainages, are often linked to elevated As in groundwater (Nordstrom and Alpers, 1999; Plumlee et al., 1999). Baños Azulmina emanates near a local mine and has the

potential to mobilize mineral deposits. This process likely explains elevated metals measured at this spring; however, it cannot account for the widespread distribution of As in the region. Naturally occurring As is less common in igneous rocks and typically highest in slates, phyllites, and black shales because of their pyrite content (Smedley and Kinniburgh, 2002). Jurassic shales and phyllites prolific throughout the CB and CH (Giovanni et al., 2010) may be a potential source for the As contribution, but more work needs to be done to constrain its provenance.

In contrast to different aqueous geochemistry exhibited by spring groups, gas compositions from all spring waters are highly variable. Group (1, 2, 3, and 4) springs plot on a mixing line between a crustal or mantle origin and air-saturated water (meteoric) (Fig. 9). Hot springs investigated in the western U.S. (Goff et al., 2002; Newell et al., 2005; Werner et al., 2008) plot similarly on the crustal/mantle – meteoric mixing line. These studies also measured $^{3}He/^{4}He$ ratios to evaluate the relative contribution of crustal and mantle sources. Additional $^{3}He/^{4}He$ data from this study is therefore necessary to further delineate fluid provenance. Appreciable amounts of H_2 gas (up to 0.3 vol. %) are also observed in hot spring waters from this study. H_2 is a primary energy source for microbial activity in hydrothermal settings, and therefore typically has a short residence time (Chapelle et al., 2002; Peterson et al., 2011). The amount of H_2 gas measured inthis study suggests the active production and flux of H_2 gas within the crust and fluids feeding CB and CH hot springs.

Considering the CBD acts as a migration channel for deeply derived fluids, we

might anticipate that this structure is also responsible for the presence of mantle-derived He measured in several Group 1 and 2 springs (Newell et al., 2015). Helium flux calculations that consider the dilution of mantle fluids by radiogenic production of He suggest that these mantle fluids are actively advecting from a present-day source at depth (Newell et al., 2015). Multiple disparities in fluid geochemistry between spring groups strongly suggest that the CBD taps and migrates deeply sourced fluids to springs in close proximity. If mantle-He volatiles behave similar to fluid geochemistry, then the CBD likely focuses and transfers mantle-He together with deep-seated fluids. Numerous studies have demonstrated the apparent relationship between elevated $^{3}He/^{4}He$ ratios and deep fracture networks (Kennedy et al., 1997; Kulongoski et al., 2003, 2005; Klemperer et al., 2015). For example, in western Anatolia, Turkey, springs emanating along the trace of the North Anatolian Fault Zone yield the highest $^{3}He/^{4}He$ ratios (Mutlu et al., 2008). Similarly, Kulongoski et al. (2013) observed decreasing $^{3}He/^{4}He$ ratios in hot springs with increasing distance from the San Andreas Fault. All of these studies attribute major strike-slip faults with deep fluid circulation, rapid transfer of mantle-He to the surface, and a lesser influence from crustal-He dilution. Aqueous geochemistry and geothermometry data from this study suggests that the deeply-penetrating CBD acts similar to these strike-slip systems in promoting deep fluid circulation. He isotope measurements from Group 3 and 4 springs are necessary to fully discern the role of the CBD in respect to mantle-He transfer. If mantle-He volatiles are indeed coupled with fluid chemistry as we suspect, then we expect substantially higher $^{3}He/^{4}He$ ratios from Group 1 and 2 springs, compared to Group 3 and 4 springs. Alternatively, if mantle-He volatiles are distributed independent of the fluid

chemistry, then we might expect similar $^{3}He/^{4}He$ ratios from all spring groups.

6. Conclusion

This study evaluates the influence of the Cordillera Blanca detachment fault (CBD) on hot spring geochemistry in the Cordillera Blanca (CB), Peru. Hot springs from a variety of locations in the Peruvian Andes were sampled and analyzed for their aqueous, gas, and stable isotope geochemistry compositions. Spring locations are geographically categorized into four groups to discern the role of the CBD as a conduit for fluid flow. Group 1 springs issue along the trace of the CBD, Group 2 springs emanate along the hanging-wall of the CBD, Group 3 springs are located in the footwall and east of the CBD, and Group 4 comprise springs south of the CBD and in the Cordillera Huayhuash (CH). Geochemistry results from Group 1 and 2 springs show similar Na-Cl dominated waters, relatively high TDS, and enrichment in $\delta^{18}O$ and δD values that collectively suggest interrelated flow-paths mixing with deep-seated hydrothermal brine. Geothermometry temperatures from Group 1 and 2 springs correspond to reservoir depths up to 10 km, thereby supporting deep circulation pathways that could accommodate mixing between meteoric recharge and Na-Cl brine. These data also support the inference of Group 2 springs issuing along steep hanging-wall normal faults that intersect the CBD at depth. Alternatively, Group 3 and 4 springs yield a wide range in water types, low TDS, and meteoric-like O and H stable isotopes that imply a greater degree of influence from shallow groundwater. Moreover, lower geothermometry temperatures and disequilibrium between cation geothermometers

support shallower circulation depths (up to 4 km) when compared to Group 1 and 2 springs. Variability in circulation depth among springs correlates with distinct fluid-rock interaction histories and can explain the disparity in Cl/Br ratios, trace element concentrations, and C stable isotope values between Groups 1 and 2 and Groups 3 and 4. We propose that the CBD fracture network is acting as a primary structural control on fluid distribution, facilitating deep flow-paths and the migration of Na-Cl brine to springs along the trace and hanging-wall of the CBD. We also suspect that the CBD is responsible for the transfer of mantle volatiles through the brittle crust to springs in Groups 1 and 2. Further He isotope data from Group 3 and 4 springs are needed to test this hypothesis. This investigation demonstrates that chemical and isotopic tracers from fault-bound hot springs are excellent tools for discerning flow-paths and determining the influence of regional tectonics on fluid distribution.

References

Antonijevic, S. K., Wagner, L. S., Kumar, A., Beck, S. L., Long, M. D., Zandt, G., Condori, C. (2015). The role of ridges in the formation and longevity of flat slabs. Nature, 524(7564), 212–215.

Arnorsson, S., Gunnlaugsson, E., and Svavarsson, H. (1983). The chemistry of geothermal waters in Iceland. III. Chemical geothermometry in geothermal investigations. Geochimica et Cosmochimica Acta, 47(3), 567-577.

Baioumy, H., Nawawi, M., Wagner, K., and Arifin, M. H. (2015). Geochemistry and geothermometry of non-volcanic hot springs in West Malaysia. Journal of Volcanology and Geothermal Research, 290, 12–22.

Banks, D. A., Giuliani, G., Yardley, B. W. D., and Cheilletz, A. (2000). Emerald mineralisation in Colombia: Fluid chemistry and the role of brine mixing. Mineralium Deposita, 35(8), 699–713.

Barazangi, M., and Isacks, B. L. (1976). Spatial distribution of earthquakes and subduction of the Nazca plate beneath South America. Geology, 4(11), 686-692.

Barnes, J. D., Sharp, Z. D., Fischer, T. P., Hilton, D. R., and Carr, M. J. (2009). Chlorine isotope variations along the Central American volcanic front and back arc. Geochemistry, Geophysics, Geosystems, 10(11).

Bellier, O., Dumont, J. F., Sébrier, M., and Mercier, J. L. (1991). Geological constraints on the kinematics and fault-plane solution of the Quiches fault zone reactivated during the 10 November 1946 Ancash earthquake, northern Peru. Bulletin of the Seismological Society of America, 81(2), 468-490.

Bense, V. F., and Person, M. A. (2006). Faults as conduit-barrier systems to fluid flow in siliciclastic sedimentary aquifers. Water Resources Research, 42(5), 1–18.

Bernal, N. F., Gleeson, S. A., Dean, A. S., Liu, X. M., and Hoskin, P. (2014). The source of halogens in geothermal fluids from the Taupo Volcanic Zone, North Island, New Zealand. Geochimica et Cosmochimica Acta, 126, 265–283.

Bethke, C. M., and Yeakel, S. (2008). The Geochemist's Workbench®—Release 7. GWB Essentials Guide. Hydrogeology Program.

Bucher, K., and Stober, I. (2010). Fluids in the upper continental crust. Geofluids, 10(1–2), 241–253.

Butcher, L. ., Mahan, K. H., and Allaz, J. M. (2017). Late Cretaceous crustal hydration in the Colorado Plateau, USA, from xenolith petrology and monazite geochronology. Lithosphere, (3), 1–18.

Caine, J. S., Evans, J. P., and Forster, C. B. (1996). Fault zone architecture and permeability structure. Geology, 24(11), 1025-1028.

Chapelle, F. H., O'neill, K., Bradley, P. M., Methé, B. A., Ciufo, S. A., Knobel, L. L., and Lovley, D. R. (2002). A hydrogen-based subsurface microbial community dominated by methanogens. Nature, 415(6869), 312.

Cobbing, E. J.; Sauchez, A. F.; Martinez, V. W.; and Zarate, O. H. 1997. Geologica de los Cuadrangulos de Huaraz, Recuay, La Union, Chiquian y Yanahuanca; hojas 20-h, 20-I, 21-I, 21-j. Bol. Inst. Geol. Minero Metalurgico Peru´ , Ser. A, Carta Geologica Nacional Rep. 76, 286 p.

Coney, P. J. (1971). Structural evolution of the Cordillera Huayhuash, Andes of Peru. Bulletin of the Geological Society of America, 82(7), 1863–1884.

Cullen, J. T., Barnes, J. D., Hurwitz, S., and Leeman, W. P. (2015). Tracing chlorine sources of thermal and mineral springs along and across the Cascade Range using halogen concentrations and chlorine isotope compositions. Earth and Planetary Science Letters, 426, 225–234.

Dansgaard, W. (1964). Stable isotopes in precipitation. Tellus, 16(4), 436–468.

Deverchere, J., Dorbath, C., and Dorbath, L. (1989). Extension related to a high topography: results from a microearthquake survey in the Andes of Peru and tectonic implications. Geophysical Journal International, 98(2), 281–292.

Doser, D. I., 1987, The Ancash, Peru, earthquake of 1946 November 10: evidence for low-angle normal faulting in the high Andes of northern Peru: Geophys. J. R. astr. Soc., v. 91, p. 57-71.

Fournier, R. O. (1977). Chemical geothermometers and mixing models for geothermal systems. Geothermics, 5(1-4), 41-50.

Fournier, R. O. (1987). Conceptual models of brine evolution in magmatic-hydrothermal systems. U.S. Geological Survey Professional Paper 1350.

Fournier, R. O., and Truesdell, A. H. (1973). An empirical Na□ K□ Ca geothermometer for natural waters. Geochimica et Cosmochimica Acta, 37(5), 1255-1275.

Garver, J. I., Reiners, P. W., Walker, L. J., Ramage, J. M., and Perry, S. E. (2005). Implications for timing of Andean uplift from thermal resetting of radiation-damaged zircon in the Cordillera Huayhuash, northern Peru. The Journal of Geology, 113(2), 117-138.

Gébelin, A., Jessup, M. J., Teyssier, C., Cosca, M. A., Law, R. D., Brunel, M., and Mulch, A. (2017). Infiltration of meteoric water in the south tibetan detachment (Mount Everest, Himalaya): When and why? Tectonics, 36(4), 690–713.

Giggenbach, W. F. (1988). Geothermal solute equilibria. derivation of Na-K-Mg-Ca geoindicators. Geochimica et cosmochimica acta, 52(12), 2749-2765.

Giggenbach, W. (1990). The chemistry of fumarolica vapor and thermal-spring discharges from Nevado del Ruiz volcanic-magmatic hydrothermal system, Colombia, 42.

Giovanni, M. K., Horton, B. K., Garzione, C. N., McNulty, B., and Grove, M. (2010). Extensional basin evolution in the Cordillera Blanca, Peru: Stratigraphic and isotopic records of detachment faulting and orogenic collapse in the Andean hinterland. Tectonics, 29(6), 1–21.

Goff, F., and Janik, C. J. (2002). Gas geochemistry of the Valles caldera region, New Mexico and comparisons with gases at Yellowstone, Long Valley and other geothermal systems. Journal of Volcanology and Geothermal Research, 116(3–4), 299–323.

Gutscher, M. A., Spakman, W., Bijwaard, H., and Engdahl, E. R. (2000). Geodynamics of flat subduction: Seismicity and tomographic constraints from the Andean margin. Tectonics, 19(5), 814-833.

Hetzel, R., Zwingmann, H., Mulch, A., Gessner, K., Akal, C., Hampel, A., ... and Wedin, F. (2013). Spatiotemporal evolution of brittle normal faulting and fluid infiltration in detachment fault systems: A case study from the Menderes Massif, western Turkey. Tectonics, 32(3), 364-376.

Hilton, D. R., Fischer, T. P., and Marty, B. (2002). Noble Gases and Volatile Recycling at Subduction Zones. Reviews in Mineralogy and Geochemistry, 47(1), 319–370.

Hoke, L., and Lamb, S. (2007). Cenozoic behind-arc volcanism in the Bolivian Andes, South America: implications for mantle melt generation and lithospheric structure. Journal of the Geological Society, 164(4), 795–814.

Hooper, E. C. D. (1991). Fluid Migration Along Growth Faults in Compacting

Sediments. Journal of Petroleum Geology, 14(October), 161–180.

Hughes, C., Jessup, M.J., Shaw, C.A., and Newell, D.L., in review, Deformation conditions during syn-convergent extension along the Cordillera Blanca Shear Zone, Peru: Geosphere.

Humphreys, E., Hessler, E., Dueker, K., Farmer, G. L., Erslev, E., and Atwater, T. (2003). How Laramide-Age Hydration of North American Lithosphere by the Farallon Slab Controlled Subsequent Activity in the Western United States. International Geology Review, 45(7), 575–595.

Kendrick, M. A., Scambelluri, M., Honda, M., and Phillips, D. (2011). High abundances of noble gas and chlorine delivered to the mantle by serpentinite subduction. Nature Geoscience, 4(11), 807–812.

Kennedy, B.M., and van Soest, M. C. (2007). Flow of Mantle Fluids Through Ductile Lower Crust: Helium Isotope Trends, 197(4300), 215–223.

Kennedy, B. M., Kharaka, Y. K., Evans, W. C., Ellwood, A., DePaolo, D. J., Thordsen, J., and Mariner, R. H. (1997). Mantle fluids in the San Andreas fault system, California. Science, 278(5341), 1278-1281.

Kesler, S. E., Martini, A. M., Appold, M. S., and Walter, L. M. (1996). Na-Cl-Br systematics of fluid inclusions from Mississippi Valley-type deposits, Appalachian Basin: Constraints on solute origin and migration paths. Geochimica et Cosmochimica Acta, 60(2), 225-233.

Klemperer, S. L., Kennedy, B. M., Sastry, S. R., Makovsky, Y., Harinarayana, T., and Leech, M. L. (2013). Mantle fluids in the Karakoram fault: Helium isotope evidence. Earth and Planetary Science Letters, 366(November), 59–70.

Klemperer, S. L., Liu, T., Hilton, D. R., Karlstrom, K. E., Crossey, L. J., and Zhao, P. (2015, December). Does the" mantle" helium signature provide useful information about lithospheric architecture of Tibet/Himalaya?. In AGU Fall Meeting Abstracts.

Kühn, M. (2004). Reactive flow modeling of hydrothermal systems (Vol. 103). Springer Science and Business Media.

Kulongoski, J. T., Hilton, D. R., Barry, P. H., Esser, B. K., Hillegonds, D., and Belitz, K. (2013). Volatile fluxes through the Big Bend section of the San Andreas Fault, California: Helium and carbon-dioxide systematics. Chemical Geology, 339(February 2013), 92–102.

Kulongoski, J. T., Hilton, D. R., and Izbicki, J. A. (2005). Source and movement of helium in the eastern Morongo groundwater Basin: The influence of regional tectonics on crustal and mantle helium fluxes. Geochimica et Cosmochimica Acta, 69(15), 3857–3872.

Leisen, M., Boiron, M. C., Richard, A., and Dubessy, J. (2012). Determination of Cl and Br concentrations in individual fluid inclusions by combining microthermometry and LA-ICPMS analysis: Implications for the origin of salinity in crustal fluids. Chemical Geology, 330–331, 197–206.

Li, L., Bonifacie, M., Aubaud, C., Crispi, O., Dessert, C., and Agrinier, P. (2015). Chlorine isotopes of thermal springs in arc volcanoes for tracing shallow magmatic activity. Earth and Planetary Science Letters, 413, 101–110.

Margirier, A., Robert, X., Audin, L., Gautheron, C., Bernet, M., Hall, S., and Simon-Labric, T. (2015). Slab flattening, magmatism, and surface uplift in the Cordillera Occidental (Northern Peru). Geology, 43(11), 1031–1034.

Margirier, A., Audin, L., Robert, X., Herman, F., Ganne, J., and Schwartz, S. (2016). Time and mode of exhumation of the Cordillera Blanca batholith (Peruvian Andes). Journal of Geophysical Research: Solid Earth, 121(8), 6235-6249.

Mark, B. G., and Mckenzie, J. M. (2007). Tracing increasing tropical Andean glacier melt with stable isotopes in water. Environmental Science and Technology, 41(20), 6955–6960.

McKenzie, J. M., Siegel, D. I., Patterson, W., and McKenzie, D. J. (2001). A geochemical survey of spring water from the main Ethiopian rift valley, southern Ethiopia: Implications for well-head protection. Hydrogeology Journal, 9(3), 265–272.

McNulty, B., and Farber, D. (2002). Active detachment faulting above the Peruvian flat slab. Geology, 30(6), 567–570.

Mégard, F. (1984). The Andean orogenic period and its major structures in central and northern Peru. Journal of the Geological Society of London, 141(5), 893–900.

Mutlu, H., Güleç, N., and Hilton, D. R. (2008). Helium-carbon relationships in geothermal fluids of western Anatolia, Turkey. Chemical Geology, 247(1–2), 305–321.

Nelson, S. T., Mayo, A. L., Gilfillan, S., Dutson, S. J., Harris, R. A., Shipton, Z. K., and Tingey, D. G. (2009). Enhanced fracture permeability and accompanying fluid flow

in the footwall of a normal fault: The Hurricane fault at Pah Tempe hot springs, Washington County, Utah. Bulletin of the Geological Society of America, 121(1–2), 236–246.

Newell, D. L., Crossey, L. J., Karlstrom, K. E., Fischer, T. P., and Hilton, D. R. (2005). Continental-scale links between the mantle and groundwater systems of the western United States: Evidence from travertine springs and regional He isotope data. GSA TODAY, 15(12), 4.

Newell, D. L., Jessup, M. J., Hilton, D. R., Shaw, C. A., and Hughes, C. A. (2015). Mantle-derived helium in hot springs of the Cordillera Blanca, Peru: Implications for mantle-to-crust fluid transfer in a flat-slab subduction setting. Chemical Geology, 417, 200–209.

Nordstrom, D. K., and Alpers, C. N. (1999). Negative pH, efflorescent mineralogy, and consequences for environmental restoration at the Iron Mountain Superfund site, California. Proceedings of the National Academy of Sciences, 96(7), 3455-3462.

Panno, S. V., Hackley, K. C., Hwang, H. H., Greenberg, S. E., Krapac, I. G., Landsberger, S., and O'Kelly, D. J. (2006). Characterization and identification of Na-Cl sources in ground water. Ground Water, 44(2), 176–187.

Pepin, J. D., Person, M., Phillips, F., Kelley, S., Timmons, S., Owens, L., … Gable, C. W. (2016). Deep fluid circulation within crystalline basement rocks and the role of hydrologic windows in the formation of the Truth or Consequences, New Mexico low-temperature geothermal system. Crustal Permeability, 155–173.

Person, M., Mulch, A., Teyssier, C., and Gao, Y. (2007). Isotope transport and exchange within metamorphic core complexes. American Journal of Science, 307(3), 555–589.

Petersen, J. M., Zielinski, F. U., Pape, T., Seifert, R., Moraru, C., Amann, R., and Pelletier, E. (2011). Hydrogen is an energy source for hydrothermal vent symbioses. Nature, 476(7359), 176.

Petford, N., and Atherton, M. (1996). Na-rich Partial Melts from Newly Underplated Basaltic Crust: the Cordillera Blanca Batholith, Peru. Journal of Petrology, 37(6), 1491–1521.

Petford, N., and Atherton, M. P. (1992). Granitoid emplacement and deformation along a major crustal lineament: The Cordillera Blanca, Peru. Tectonophysics, 205(1–3), 171–185.

Pilger JR, R. H. (1981). Plate reconstructions, aseismic ridges, and low-angle subduction beneath the Andes. Geological Society of America Bulletin, 92(7), 448-456.

Piper, A. M., 1944, A graphical procedure in the geochemical interpretation of water analyses: Transactions (American Geophysical Union), v. 25, p. 914-923.

Plumlee, G. S., Smith, K. S., Montour, M. R., Ficklin, W. H., and Mosier, E. L. (1999). Geologic controls on the composition of natural waters and mine waters draining diverse mineral-deposit types. The environmental geochemistry of mineral deposits. Part B: case studies and research topics, 6, 373-432.

Ramos, V. a., and Folguera, a. (2009). Andean flat-slab subduction through time. Geological Society, London, Special Publications, 327(1), 31–54.

Rosenbaum, G., D. Giles, M. Saxon, P. G. Betts, R. F. Weinberg, and C. Duboz (2005), Subduction of the Nazca Ridge and the Inca Plateau: Insights into the formation of ore deposits in Peru, Earth Planet. Sci. Lett., 239,18–32.

Salata, G. G., Roelke, L. A., and Cifuentes, L. A. (2000). A rapid and precise method for measuring stable carbon isotope ratios of dissolved inorganic carbon. Marine Chemistry, 69(1-2), 153-161.

Sano, Y., and Marty, B. (1995). Origin of carbon in fumarolic gas from island arcs. Chemical Geology, 119(1-4), 265-274.

Sharp, Z. (2007). Principles of stable isotope geochemistry. Upper Saddle River, NJ: Pearson education p. 344.

Sharp, Z. D., and Barnes, J. D. (2004). Water-soluble chlorides in massive seafloor serpentinites: A source of chloride in subduction zones. Earth and Planetary Science Letters, 226(1–2), 243–254.

Smedley, P. L., and Kinniburgh, D. G. (2002). A review of the source, behaviour and distribution of arsenic in natural waters. Applied Geochemistry, 17(5), 517–568.

Werner, C., Hurwitz, S., Evans, W. C., Lowenstern, J. B., Bergfeld, D., Heasler, H., … Hunt, A. (2008). Volatile emissions and gas geochemistry of Hot Spring Basin, Yellowstone National Park, USA. Journal of Volcanology and Geothermal Research, 178(4), 751–762.

Yokoyama, T., Nakai, S., and Wakita, H. (1999). Helium and carbon isotopic compositions of hot spring gases in the Tibetan Plateau. Journal of Volcanology and Geothermal Research, 88(1–2), 99–107.

APPENDICES

Appendix A

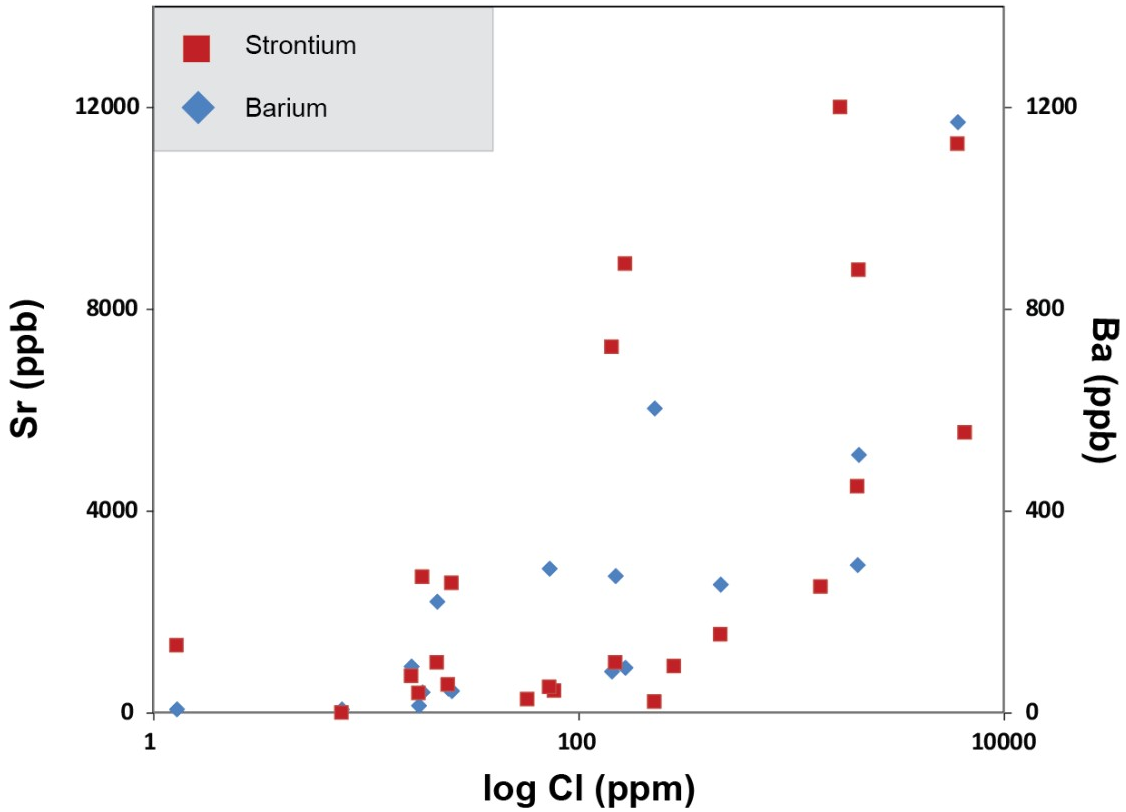

Figure A1. Strontium (red) and barium (blue) vs. log chlorine concentration from hot springs located proximal and distal to the Cordillera Blanca detachment. Both trace elements exhibit a positive relationship with increasing chlorine.

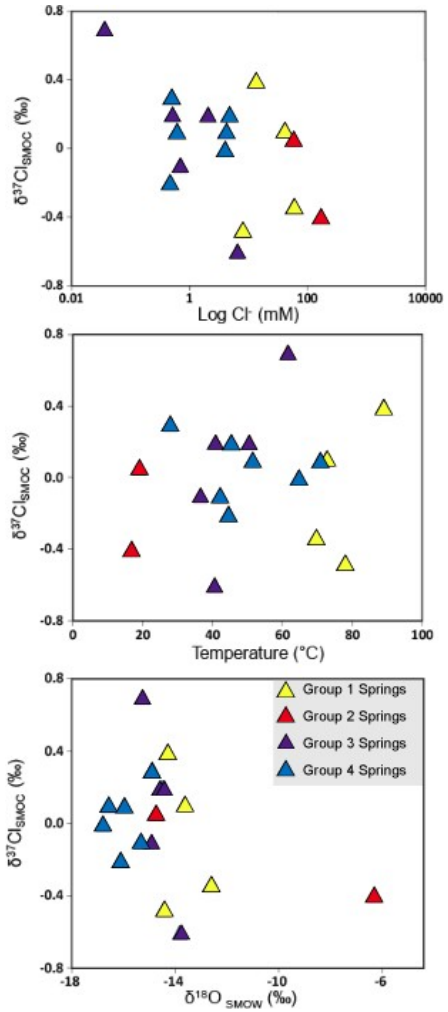

Figure A2. $o^{37}Cl$ values from hot springs proximal and distal to the Cordillera Blanca detachment, as a function of log Cl^- concentration (top), spring surface temperature (middle), and $o^{18}O$ values (bottom). No obvious trends are observed.

Appendix B: Thermal spring location and aqueous geochemistry data

Table A1. Sample ID, location, and field parameters for hot springs in the Cordillera Blanca and Cordillera Huayhush, Peru.

Group/Location (Baños)	Sample ID	Latitude	Longitude	Elevation (m)	T (°C)	pH	Cond. (uS)
Group 1							
Huancarhuaz	DN13CB11	-8.94365	-77.78461	2721	73.3	6.22	5120
Aquilina	DN13CB14	-8.61294	-77.88359	1930	78.3	6.26	2130
Huancarhuaz	DNCB15-08	-8.9415	-77.7853	2721	69.9	6.4	5750
Pacatque	DNCB15-10	-8.61294	-77.88359	-	88.9	6.84	2280
Group 2							
Olleros 2b	DN13CB05	-9.6683	-77.46262	3453	20.4	6.56	23200
Olleros 4	DN13CB06	-9.6673	-77.46327	3432	47.8	6.49	21500
Merced	DN13CB07	-9.2591	-77.61185	3002	38.4	5.03	723
Chancos	DN13CB08b	-9.31958	-77.57518	2863	47.6	6.22	6020
Monterrey	DN13CB09	-9.46841	-77.53543	2983	46.4	5.89	6240
Shangol	DN13CB13	-8.98458	-77.81697	2214	39.6	6.01	1025
Pumapampa	DNCB15-12	-9.880278	-77.286389	4185	19.2	5.95	3970
Recuay	DNCB15-13	-9.718	-77.459	-	16.9	6.81	14380
Group 3							
Aticara	DNCB15-11	-8.6125	-77.8836	2662	36.6	8.87	170
Pomabamba	DNCB17-2	-8.826	-77.46	2910	50.5	6.62	468.2
Chihuan	DNCB17-6	-8.672	-77.634	3304	36.5	7.02	606.6
Rupac	DNCB17-9	-8.595	-77.566	2443	61.5	6.18	229.5
Jocos Peinado	DNCB17-13	-8.295	-77.488	1591	40.6	6.31	3332
Chavin	DNCB17-21	-9.611	-77.182	3214	41	7.47	1406
Group 4							
Conococha	DNCB17-24	-10.129	-77.289	4026	28	7.98	233.1
Azulmina	DNCB17-25	-9.938	-76.963	3870	70.7	5.96	1452
Taurimpampa	DNCB17-30	-9.847	-76.817	3244	45.3	6.24	1387
Banos (Batan)	DNCB17-32	-10.048	-76.722	3390	64.7	5.71	940.3
Conoc (La Union)	DNCB17-36	-9.781	-76.805	3175	42.2	6.68	376.7
Machaycancha (Conog)	DNCB17-37	-10.164	-76.811	3835	44.6	6.4	567.6
Janac	DNCB17-38	-10.154	-76.902	4343	51.5	6.48	720.3

- not determined

Table A2. Major element concentrations (ppm) for Cordillera Blanca and Cordillera Huayhuash hot springs.

Group/Location (Baños)	Sample ID	Na	Mg	K	Ca	HCO_3	Cl	SO_4	Si	Charge Balance (%)	Quartz S.I. [a]	Calcite S.I. [a]
Group 1												
Huancarhuaz	DN13CB11	1164	2.74	162.5	70	779.6	1468	38.4	79	3	0.8	-0.3
Aquilina	DN13CB14	431	1.22	28.1	29.5	488.8	282	148	48.9	5	0.5	-0.6
Huancarhuaz	DNCB15-08	1299.7	4.46	198.89	114.2	805.4	2080.27	46.09	-	-4	-	0.1
Pacatque	DNCB15-10	562.03	1.78	47.96	46.81	646.8	467.13	189.15	-	1	-	0.5
Group 2												
Olleros 2b	DN13CB05	4948	48	694	330	2103	7369	16	-	2	-	0.2
Olleros 4	DN13CB06	4714	38.2	690	285	2029.5	6553	85	-	4	-	0.5
Merced	DN13CB07	82.07	9.4	11.8	33.04	259.9	76.5	9.6	16.1	0	0.6	-3.4
Chancos	DN13CB08b	1079	17.3	175.9	150.8	952.9	1372	111	49.5	3	0.9	-0.2
Monterrey	DN13CB09	1297	9.77	174.2	51.4	538.3	1708	3.32	-	6	-	-1.4
Shangol	DN13CB13	223	12.9	22.8	73.6	191.8	57.5	384	16.7	8	0.6	-1.6
Pumapampa	DNCB15-12	675.99	49.11	162.33	252.47	1000.7	2054.69	15.39	-	-20	-	-0.9
Recuay	DNCB15-13	3222.86	76.84	362.47	351.29	2257.6	6019.81	45.31	-	-9	-	0.6
Group 3												
Aticara	DNCB15-11	45.19	0.15	0.74	4.05	67.1	7.75	41.24	-	1	-	0.2
Pomabamba	DNCB17-2	45.41	10.84	7.24	19.95	198	18.37	25.41	29.43	-3	0.6	-0.9
Chihuan	DNCB17-6	62.77	5.5	3.47	47.88	173.3	24.39	120.35	17.64	-3	0.6	-0.3
Rupac	DNCB17-9	9.79	7.58	3.18	12.88	61.9	1.29	49.74	23.2	-6	0.4	-2
Jocos Peinado	DNCB17-13	114.44	108.05	30.83	535.99	371.2	227.65	1451.64	10.27	-2	0.2	-0.2
Chavin	DNCB17-21	67.3	42.04	8.16	191.58	532.1	72.84	267.49	9.7	-1	0.3	-0.2
Group 4												
Conococha	DNCB17-24	24.79	2.14	2.29	15.97	99	17.69	1.35	10.21	-1	0.5	0
Azulmina	DNCB17-25	98.01	24.19	17.83	120.36	315.6	150.07	211.1	27.59	-4	0.4	-0.8
Taurimpampa	DNCB17-30	96.43	14.6	18.14	111.26	525.9	165.14	29.53	25.35	-10	0.2	-0.4
Banos (Batan)	DNCB17-32	97.49	12.02	17.46	49.33	247.5	143.11	17.56	18.41	-2	0.3	-1.6
Conoc (La Union)	DNCB17-36	18.73	10.85	3.73	32.63	123.7	25.32	22.55	13.55	3	0.4	-0.9
Machaycancha (Conog)	DNCB17-37	21.74	9.15	6.23	70.65	160.9	16.39	122.34	21.43	-2	0.6	-0.9
Janac	DNCB17-38	20.09	10.82	6.68	91.65	198	21.67	184.46	38.84	-8	0.8	-0.5

- not determined; [a] saturation index defined as the log[ion activity product(IAP)/solubility product(Ksp)]; calculated using Geochemist's Workbench (Bethke, 2008).

Table A3. Trace element concentrations (ppb) for Cordillera Blanca and Cordillera Huayhuash hot springs.

Sample ID	Be	Al	V	Cr	Mn	Fe	Co	Ni	Cu	Zn	As	Se	Sr	Cd	Sb	Ba	Ti
Group 1																	
DN13CB11	5.62	-	2.31	-	443	449	-	-	1.73	-	1655	3.04	-	-	36	646	9.28
DN13CB14	3.83	29.7	-	-	77.4	399	-	-	-	5.91	1496	-	-	-	21.7	91.8	1.18
DNCB15-08	12.36	2.23	-	-	566.26	1111.1	-	-	-	6.81	1851.21	2.31	5099.29	-	40.41	876.37	15.09
DNCB15-10	8.73	12.1	-	-	109.76	607.17	-	-	-	6.1	2634.25	-	2544.08	-	39.48	153.88	2.25
Group 2																	
DN13CB05	1.04	41.4	6.12	0.43	411	12345	-	1.13	16.6	-	2107	7.46	-	-	0.26	1123	-
DN13CB06	1.29	46.5	5.87	0.32	347	6570	-	0.91	15.3	-	10806	6.88	-	-	0.35	554	1.35
DN13CB07	0.62	-	-	-	1096	8565	-	-	-	6.33	2.37	-	-	-	-	43.6	-
DN13CB08b	1.67	-	2.7	-	180	197	-	-	1.67	-	622	2.36	-	-	6.29	249	0.5
DN13CB09	0.55	-	2.06	-	1787	155	-	-	1.98	-	1.26	3	-	-	0.25	1200	0.02
DN13CB13	3.7	-	-	-	2931	1957	13.7	19.3	-	5532	390	-	-	1.47	179	24.6	17
DNCB15-12	6.46	212.54	-	-	1709	8452.14	0.32	0.91	-	6.05	9.37	0.19	2913.41	-	-	447.4	-
DNCB15-13	0.52	2.01	-	-	1077	193.71	-	-	-	-	4.05	1.9	11697.83	-	-	1126.21	-
Group 3																	
DNCB15-11	-	20.73	0.73	-	0.24	-	-	0.51	2.23	8.04	38.25	-	61	-	-	-	-
DNCB17-2	0.08	-	-	-	161	18.31	-	-	-	-	4.13	-	412.36	-	-	268.32	-
DNCB17-6	0.08	1.86	-	-	297	-	-	-	-	2.39	2.28	-	482.32	-	-	55.35	-
DNCB17-9	-	0.82	-	-	316	2287.25	0.17	-	-	10.03	16.53	-	71.82	-	-	133.16	0.11
DNCB17-13	4.75	2.48	-	1.2	4.58	59.58	-	-	-	-	210.19	-	6022.82	-	-	21.43	-
DNCB17-21	0.07	1.54	-	-	160.26	50.38	0.36	-	-	3.86	0.76	-	2844.48	-	10.92	49.1	0.22
Group 4																	
DNCB17-24	-	2.72	-	-	57.78	190.45	-	-	-	3	36.35	-	139.95	-	-	36.73	-
DNCB17-25	0.75	8.74	-	-	873.78	1915.84	-	-	-	12.43	9.07	-	2702.39	-	6.89	99.54	2.76
DNCB17-30	0.08	1.42	-	18.63	76.13	307.05	-	-	1.18	3.94	125.67	-	896.94	-	5.81	889.15	0.19
DNCB17-32	0.19	4.64	-	-	316.4	266.91	-	-	-	2.96	244.67	-	825.1	-	12.81	723.07	1.95
DNCB17-36	-	2.39	-	-	179.58	113.29	-	-	-	-	52.69	-	436.81	-	3.42	255.9	-
DNCB17-37	0.14	0.68	-	-	333.83	458.37	-	-	-	3.45	597.83	-	916.47	-	3.84	72.79	-
DNCB17-38	0.08	4.03	-	-	189.87	387.6	-	-	-	-	17.29	-	2200.1	-	-	98.38	-

- below detection limit

Table A4. Oxygen and hydrogen stable isotope ratios for hot springs and meteoric water in the Cordillera Blanca and Huayhuash.

Location	Sample ID	Latitude	Longitude	Elevation (m)	$\delta^{18}O$ (‰) SMOW	δD (‰) SMOW
Group 1						
Baños Huanacarhuaz	DN13CB11	-8.94365	-77.78461	2721	-13.33	-103.7
Baños Aquilina	DN13CB14	-8.61294	-77.88359	1930	-14.21	-107.27
Baños Huancarhuaz	DNCB15-7	-	-	-	-13.64	-105.92
Baños Huancarhuaz	DNCB15-8	-8.9415	-77.7853	2721	-12.6	-94.4
Baños Aqulina	DNCB15-9b	-8.61294	-77.88359	1884	-14.44	-112.85
Baños Pacatque	DNCB15-10	-8.6125	-77.8836	-	-14.29	-102.62
Group 2						
Baños Olleros 1	DN13CB04	-9.66857	-77.46303	3464	-7.75	-81.1
Baños Olleros 2b	DN13CB05	-9.6683	-77.46262	3453	-6.42	-74.3
Baños Olleros 4	DN13CB06	-9.6673	-77.46327	3432	-4.93	-79.8
Banos Merced	DN13CB07	-9.2591	-77.61185	3002	-12.6	-94.4
Baños Chancos	DN13CB08b	-9.31958	-77.57518	2863	-10.48	-85.9
Baños Monterrey	DN13CB09	-9.46841	-77.53543	2983	-10.22	-87.7
Baños Shangol	DN13CB13	-8.98458	-77.81697	2214	-12.96	-98.5
Baños Pumapampa	DNCB15-12	-9.880278	-77.286389	4185	-14.74	-110.96
Baños Recuay	DNCB15-13	-9.718	-77.459	-	-6.31	-78.79
Group 3						
Baños Aticara	DNCB15-11	-8.6125	-77.8836	2662	-13.07	-93.92
Baños Pomabamba	DNCB17-1	-8.82545	-77.45945	2901	-14.31	-104.2
Baños Pomabamba	DNCB17-2	-8.826	-77.46	2910	-14.46	-110.08
Baños Chilhuan	DNCB17-6	-8.672	-77.634	3304	-14.92	-109.73
Baños Rupac	DNCB17-7b	-8.596	-77.568	2360	-15.16	-107.31
Baños Rupac	DNCB17-9	-8.595	-77.566	2443	-15.26	-112.55
Baños Jocos Peinado	DNCB17-13	-8.295	-77.488	1591	-13.83	-103.3
Baños Chavin	DNCB17-21	-9.611	-77.182	3214	-14.57	-116.05
Group 4						
Baños Conococha	DNCB17-24	-10.129	-77.289	4026	-14.9	-117.81
Baños Azulmina	DNCB17-25	-9.938	-76.963	3870	-15.97	-123.85
Baños Taurimpampa	DNCB17-30	-9.847	-76.817	3244	-14.44	-114.49
Baños (Batan)	DNCB17-32	-10.048	-76.722	3390	-16.81	-129.91

Baños Conoc (La Union)	DNCB17-36	-9.781	-76.805	3175	-15.32	-118.24
Baños Machaycancha (Conog)	DNCB17-37	-10.164	-76.811	3835	-16.12	-120.29
Baños Janac	DNCB17-38	-10.154	-76.902	4343	-16.58	-125.35
Cold meteoric water						
Lag. Quesho	DNCB15-5	-9.08822	-77.69595	3482	-14.42	-103.35
Rio Pomabamba	DNCB17-3	-8.824616	-77.4608	2893	-14.44	-95.33
Rio Sihuas	DNCB17-8	-8.596	-77.568	2360	-13.92	-104.32
Pond Above Quiches	DNCB17-20	-8.462683	-77.501883	3214	-6.37	-70.02
Rio Mosna	DNCB17-22	-9.61075	-77.182183	3205	-15.21	-119.8
Rio Azulmina	DNCB17-26	-9.938	-76.963	3870	-15.4	-118.68

Table A5. Halogen data (Cl, Br, $o^{37}Cl$) from Cordillera Blanca and Cordillera Huayhuash hot springs.

Location	Sample ID	Cl (mM)	Br (mM)	Cl/Br	$o^{37}Cl$ (‰) SMOC
Group 1					
Baños Huancarhuaz	DNCB15-7	41.41	0.0373	1109	0.1
Baños Huancarhuaz	DNCB15-8	58.67	0.0511	1148	-0.3
Baños Aqulina	DNCB15-9b	7.93	0.0127	626	-0.5
Baños Pacatque	DBCB15-10	13.17	0.0153	861	0.4
Group 2					
Baños Pumapampa	DNCB15-12	57.97	0.0411	1410	0.1
Baños Recuay	DNCB15-13	169.82	0.1636	1038	-0.4
Group 3					
Baños Pomabamba	DNCB17-2	0.52	0.0023	228	0.2
Baños Chilhuan	DNCB17-6	0.69	0.0006	1095	-0.1
Baños Rupac	DNCB17-9	0.04	0.0001	468	0.7
Baños Jocos Peinado	DNCB17-13	6.42	0.0149	430	-0.6
Baños Chavin	DNCB17-21	2.05	0.0052	394	0.2
Group 4					
Baños Conococha	DNCB17-24	0.5	0.0009	575	0.3
Baños Azulmina	DNCB17-25	4.23	0.0124	341	0.1
Baños Taurimpampa	DNCB17-30	4.66	0.0141	331	0.2
Baños (Batan)	DNCB17-32	4.04	0.0137	294	0
Baños Conoc (La Union)	DNCB17-36	0.71	0.0017	426	-0.1

Baños Machaycancha (Conog)	DNCB17-37	0.46	0.0011	407	-0.2
Baños Janac	DNCB17-38	0.61	0.001	586	0.1

Table A6. Gas composition (mole % in mmol/mol) for Cordillera Blanca and Cordillera Huayhuash hot springs.

Location	**Sample ID**	**CO_2**	**Ar**	**N_2**	**CH_4**	**H_2**	**He**	**CO**	**O_2**
Group 1									
Baños Huancarhuaz	DNCB15-7	93.7	0.083	5.3	0.001	0.1	0.18	0.01	0.624
Baños Huancarhuaz	DNCB15-8	74.9	0.378	23.9	0.01	0.21	0.0319	0.011	0.491
Baños Aqulina	DNCB15-9b	10.7	2.21	86.5	0.003	0.04	0.0466	-	0.538
Group 2									
Baños Pumapampa	DNCB15-12	96	0.167	3	0.019	0	0.4387	-	0.354
Group 3									
Baños Aticara	DNCB15-11	17.2	1.91	80.6	-	0.03	0.0846	-	0.112
Baños Chilhuan	DNCB17-6	38.9	1.62	56.2	0.402	0.046	0.544	-	2.24
Baños Rupac	DNCB17-7b	53.4	0.857	40.9	0.718	0.039	-	-	4.05
Baños Jocos Peinado	DNCB17-13	76.6	0.593	21.6	0.036	0.031	-	-	1.1
Baños Chavin	DNCB17-21	48.8	0.919	48.9	0.01	0.331	0.2823	-	0.79
Group 4									
Baños Azulmina	DNCB17-25	95.4	0.092	3.61	0.022	0.004	0.0933	-	0.789
Baños Taurimpampa	DNCB17-30	87.2	0.34	11.6	0.018	0.019	0.1026	-	0.682

- not determined